CHEMISTRY OF MATERIALS

pubs.acs.org/cm

Article

Extreme Ultraviolet and Beyond Extreme Ultraviolet Lithography Using Amorphous Zeolitic Imidazolate Resists Deposited by Atomic/Molecular Layer Deposition

Kayley E. Waltz, Xinpei Zhou, Xavier Krull, Somya Singh, Eric Mattson, Yurun Miao, Matt Hettermann, Travis Grodt, Qi Zhang, Honggu Im, Bernhard Lüttgenau, Lauren Doyle, Andrea Kraetz, Max Beutner, Scott B. Clendenning, D. Howard Fairbrother, Joseph T. Hupp, Patrick Naulleau, Lawrence Rooney, Oleg Kostko,* and Michael Tsapatsis*

Cite This: *Chem. Mater.* 2025, 37, 8548–8567

Read Online

ACCESS | Metrics & More | Article Recommendations | Supporting Information

ABSTRACT: Amorphous zinc-imidazolate (aZnMIm) resists show potential to meet the demands for next-generation high-numerical aperture (high-NA) metal-containing extreme ultraviolet (EUV) resist materials, given their ease of deposition by atomic/molecular layer deposition (ALD/MLD) at thicknesses of 20 nm and below. This study demonstrates that aZnMIm thin films, previously identified as high-resolution electron beam resists, can also function as negative-tone EUV photoresists. Water development achieves high sensitivity (5 mJ/cm^2) but leaves significant residue, while acetic acid development results in poor contrast. A hybrid approach—water followed by acetic acid—enables residue-free development with a sensitivity of 181 mJ/cm^2. Dry development using 1,1,1,5,5,5-hexafluoroacetylacetone (hfacH) is also possible but shows lower sensitivity (375 mJ/cm^2) compared to wet development methods. EUV photoelectron spectroscopy (PES), reflectometry/EUV absorption, total electron yield (TEY), residual gas analysis (RGA), and time-of-flight secondary ion mass spectrometry (TOF-SIMS) were used to investigate the effects of EUV irradiation on aZnMIm resists. Reflectometry experiments reveal an aZnMIm EUV absorption coefficient of 6.2 μm^{-1}, while PES and TEY analyses show that, compared to poly(4-hydroxystyrene) (PHS), a polymer-based reference resist, aZnMIm emits more primary and secondary electrons but generates fewer slow electrons relative to its primary electron emission; its total electron yield is similar to that of poly(methyl methacrylate) (PMMA) resists. When exposed to EUV, aZnMIm predominantly outgasses H_2, as determined by RGA. TOF-SIMS measurements demonstrate that high-dose EUV exposure only partially fragments the 2-methylimidazole (2MIm) organic linkers, unlike high-dose electron beam exposure, which is known to completely degrade them. Additionally, aZnMIm resists show promise for potential beyond EUV lithography (BEUVL) due to the presence of Zn, which provides higher sensitivity at a wavelength of 6.7 nm compared to other metal ions, such as Sn, that are currently used in the best-performing EUV metal−organic resists. TEY measurements demonstrate that aZnMIm emits nearly twice as many electrons as PHS at 6.7 nm. The BEUV TEY of aZnMIm also surpasses that of PMMA, poly(pentafluorostyrene), and poly(4-iodostyrene), with the latter two being known for their high EUV TEYs. This work provides insight into zeolitic imidazolate framework (ZIF)-based EUV and BEUV resists and highlights their potential for both wet and dry development.

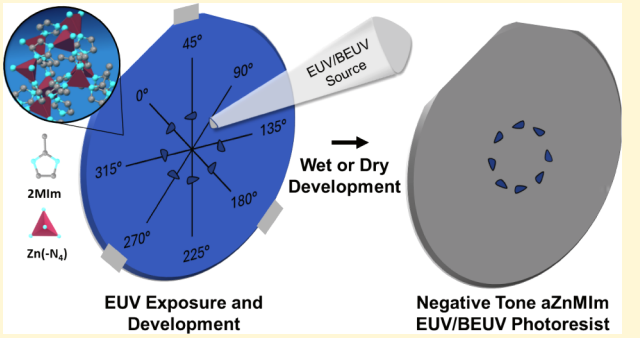

INTRODUCTION

Microchips, which are crucial for powering modern electronics, rely on the interplay of billions of transistors, each meticulously fabricated through a series of intricate engineering processes. Lithography is an essential process in the fabrication of microelectronic devices. It uses a thin sacrificial layer, called a photoresist or simply resist, typically deposited using solvent-based spin-coating methods, to transfer integrated circuit (IC) patterns to the surface of a semiconductor material of interest. To sustain the demand for denser ICs, excimer lasers have been replaced by plasma sources emitting extreme ultraviolet (EUV) light (λ = 13.5 nm, 92 eV) because the use of shorter wavelengths improves spatial resolution in patterning.[1−3] In the case of EUV light, radiation absorbed in exposed areas of the resist produces primary photoelectrons, which lose energy

Received: June 11, 2025
Revised: October 5, 2025
Accepted: October 7, 2025
Published: October 30, 2025

and generate a cascade of low-energy secondary electrons (LESEs, energies <20 eV).[4,5] These secondary electrons initiate reactions that enable pattern development, usually as a result of solubility switching, which is then typically exploited by washing the resist with solvents.[5,6] State-of-the-art EUV lithography (EUVL) is the current top-down lithographic technology for creating the dense nanopatterns needed for the miniaturization of components for efficient microelectronics.[3,7] Shorter wavelengths at 6.7 nm and lower, called beyond EUV (BEUV), have been proposed for next-generation patterning, although there is no clear roadmap for implementation at this time.[8]

Despite significant advantages and recent commercialization, several issues potentially limit the further scaling of EUVL to the high-numerical aperture (high-NA) regime supporting direct patterning at the sub-22 nm pitch level.[3] One of the challenges is the design of resist materials that are sufficiently EUV-sensitive.[9,10] To address the low EUV sensitivity of organic resists, there has been a shift toward inorganic or hybrid inorganic−organic resist materials, such as metal-oxide and metal−organic resists, that contain transition metals or other metals with higher EUV optical density compared to typical organic polymer-based resists.[9,11] In addition to increased EUV sensitivity, metal-based resists also lead to improved resolution and other resist properties such as etch resistance.[6,10−15] Therefore, resist systems have emerged containing metals such as Sb, Zr, Zn, Hf, In, and Sn[16−25] incorporated as metal-oxo clusters and organometallic carboxylates with polymerizable substituents,[16,20,26−30] nanoparticles capped with organic ligands,[9,31,32] metal-infiltrated polymers,[33,34] or low-carbon-containing metal nitrate hydrate films.[25] Notable high-resolution performance has been reported for tin-oxo cluster-based resists of the type $[(RSn)_{12}O_{14}(OH)_6]X_2$[20,30] and is attributed to the high density of Sn atoms exhibiting strong EUV-photon absorption.[35]

Metal−Organic Frameworks (MOFs), which are a versatile class of materials with applications in catalysis,[36,37] gas separation and sorption,[38,39] sensing,[40,41] and low-k dielectrics,[42] have also recently shown potential as high-resolution patternable metal-containing materials.[19,43−48] As a subclass of MOFs, Zeolitic Imidazolate Frameworks (ZIFs) stand out due to their diverse topologies and compositions, which can be synthesized through well-established solvothermal and vapor-phase methods.[49−53] In 2018, it was discovered that ZIFs exhibit distinct dissolution behavior between irradiated and nonirradiated regions, enabling their use in electron beam lithography (EBL).[43] Since then, both negative- and positive-tone EBL patterning has been demonstrated in crystalline[43−46,54] and, more recently, amorphous ZIFs.[47,48]

Metal-based resists have, however, encountered several challenges, specifically with the transition toward high-NA EUVL. Specifically, the Rayleigh depth-of-focus decreases significantly with increasing NA, requiring thinner resists (from ca. 30 to 15 nm or below) to maintain a well-focused aerial image throughout the full resist thickness to produce high-resolution, densely spaced patterns.[55−57] As the thickness of resist layers decreases, issues like resist inhomogeneity stemming from natural molecular size, random density fluctuations, and component aggregation and segregation are magnified.[55] Consequently, small molecular unit, metal-containing resist materials exhibiting superior sensitivity and resolution, minimal roughness, and facile homogeneous deposition at an ultrathin scale must be developed to meet the increasing stringent demands of the semiconductor industry.[15,55,58,59]

In parallel to the urgent need for EUVL resists to meet technological demands, increased emphasis to develop eco-friendly manufacturing processes has stimulated efforts toward all-dry resists, eliminating the need for aqueous and organic solvents. Metal-based EUV resists can also be more environmentally friendly materials, given that they generally do not contain perfluoroalkyl and polyfluoroalkyl substances (PFAS) present in organic polymer-based chemically amplified resists (CARs). Moreover, all-dry metal-based resists have the potential to remove the requirement for extra baking steps and stabilization agents/adhesion promoters often required for spin-coated resists, reduce pattern collapse caused by capillary forces during wet development, and lower processing costs and waste production by 5−10x due to the significant reduction in the amount of solvent waste generated.[21,22,44,46,48,60] The advantages of dry over wet development processes become even more significant as the demands for pattern resolution continue to increase. Although dry development and etching techniques based on plasma reactive ion etching (RIE) have been explored, plasma etching requires a high etch resistance of the photoresist and other materials present in the microelectronic device.[61] Consequently, selective, nonplasma-based dry developing agents are required for continued advancement of all-dry lithographic processing. Indeed, Lam Research Corporation introduced one example of an all-dry resist system in 2021[21−24] and demonstrated enhanced photon absorption, reduced processing steps, higher yield, reduction in pattern defects, as well as improvements in feature blurring and the formation of complex high-aspect-ratio pillars.[22,62,63] In 2022, Lam Research announced that SK Hynix Inc. had chosen their dry resist technology for the production of advanced DRAM chips,[62] and in 2025, they announced that their dry resist, now called Aether, was selected by another leading memory manufacturer as a production tool of record to enable advanced DRAM processes for high-volume manufacturing (HVM).[63] Their work has demonstrated that all-dry processes are industrially desirable and feasible for EUVL-based semiconductor HVM. Although lithography resists that can be deposited and developed from the vapor-phase offer the aforementioned advantages, they face challenges in industrial settings because most standard lithography processes rely on spin-coating from precursor solutions and the use of liquid-phase developers.[64,65] Furthermore, for research and development requiring rapid exploration of resist compositions, the ability to deposit and develop films via combinations of vapor- or liquid-phase processing can be highly beneficial. For these reasons, exploring resist families amenable to a wide range of deposition and development processing conditions is currently pursued.[44,48,66]

In a previous report, we presented an all-dry resist deposition and development process that utilizes ZIF-inspired amorphous zinc-imidazolate (aZnMIm) films deposited by atomic/molecular layer deposition (ALD/MLD), hereafter referred to as MLD, patterned with EBL, and developed by vapor-phase etching at 120 °C using 1,1,1,5,5,5-hexafluoroacetylacetone (hfacH) to achieve well-resolved 22 nm lines with a pitch of 30 nm.[48] With the use of underlayers, we later demonstrated well-resolved 16 nm thick, 20 nm pitch lines.[67] This is the first fully documented nonplasma-based all-dry process capable of producing high-fidelity patterns from metal-

https://doi.org/10.1021/acs.chemmater.5c01476
Chem. Mater. 2025, 37, 8548−8567

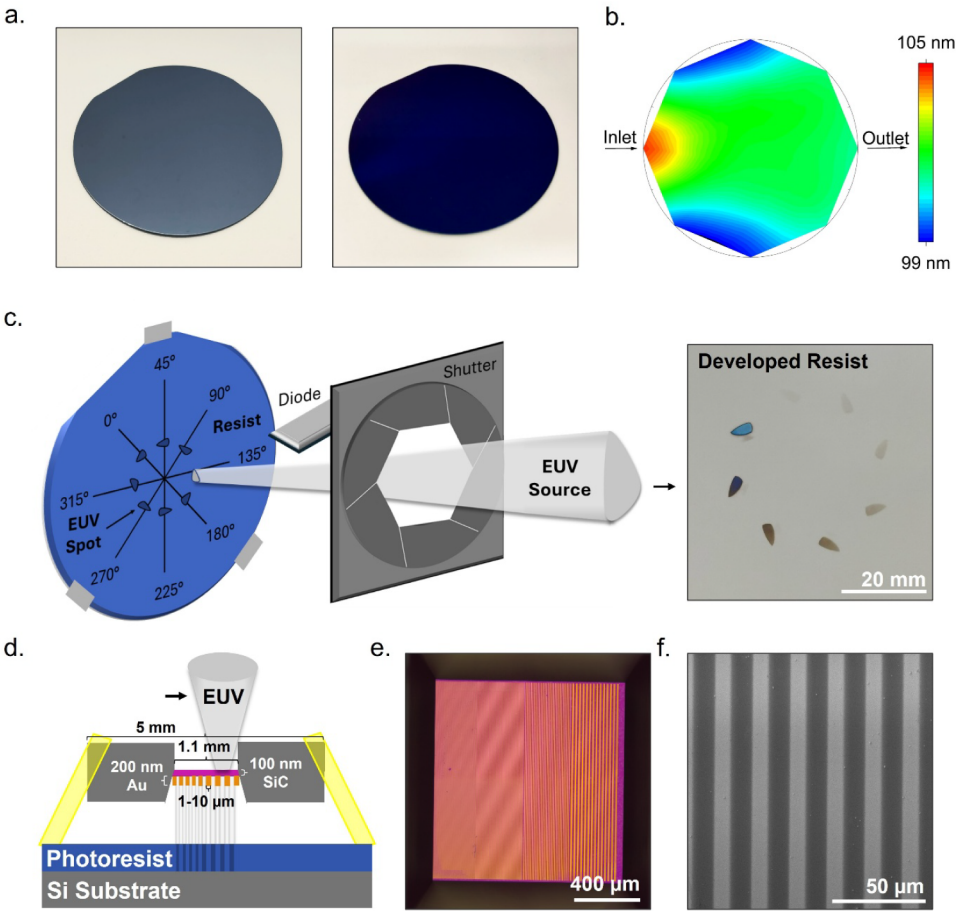

Figure 1. EUV lithography using aZnMIm resists. (a) 100 mm diameter Si (100) wafer before (left) and after (right) MLD (650 cycles) of aZnMIm. (b) Height contour plot showing the spatial uniformity of the film deposited in (a). (c) EUV exposure schematic showing the shutter open and the diode rotated out of the measurement position so that the EUV source is exposing the photoresist at a rotation angle of 135°. To expose, the wafer is tightened into the holder, and a recipe is loaded with the time for the shutter to be open at each of the eight angles marked on the schematic. Once the recipe is started, the wafer rotates to the correct angle, and the shutter is opened, allowing EUV light to expose the photoresist for a desired amount of time. The shutter is closed, and then, the wafer rotates to the next position to repeat until all eight spots have been exposed (left). The diode is inserted before and after the recipe to measure the current and calculate the EUV dose. Once the wafer is removed from the chamber, it was developed in an appropriate solvent or vapor to reveal the exposure spots (right). The development in (c) was conducted using hfacH vapor at 120 °C for 60 s and is reported in a later section as Figure 2f. (d) Schematic depicting line fabrication using an EUV flood exposure tool and a coarse grating mask. A cross-section of the mask is shown taped to the photoresist-coated wafer. The mask is composed of a 100 nm thick SiC membrane with 200 nm thick electroplated Au gratings of varying width (1−10 μm). The same EUV source as in (c) is swept over the mask, exposing the photoresist in areas that are not blocked by Au lines. (e) A top-down optical microscope image of the mask, which has four grating sizes, 1, 2, 5, and 10 μm, with pitches of 2, 4, 10, and 20 μm, respectively. (f) SEM image of 10 μm lines patterned in a 102 nm thick aZnMIm resist using the mask and method described in parts (e) and (d) and developed using solvent-based methodology. A dose of 293 mJ/cm^2 was used for patterning. After EUV exposure, the film was developed in DI water for 5 min and then in 655 μM acetic acid for 2 min. The choice of developer is discussed in the next section of this paper and is shown in Figure 2a−c.

containing resists in the open literature. Consequently, aZnMIm resists have the potential to meet the technological demands of IC patterning while simultaneously reducing the environmental impact of EUVL through waste reduction. As other investigations have focused on the use of electron-beam, X-ray, or UV lithography,[43−45,47,48,68] the use of amorphous zeolitic imidazolate framework-based materials as EUV resists has not been demonstrated in the literature. Very recently, Li et al. explored EUV exposure of ZIFs for the first time with resist-free positive-tone EUV patterning of halogenated crystalline ZIFs yielding resolution down to 40 nm half-pitch, highlighting EUV-induced modifications driven by chlorine-based chemistries.[69]

In this study, we explore the viability of aZnMIm as a resist for EUV lithography. The aZnMIm films are deposited using MLD, subjected to EUV exposure, and then developed using both liquid- and vapor-phase techniques. We show that these aZnMIm resists exhibit sensitivity to EUV light and can be successfully developed in both the liquid- and vapor-phases. Moreover, this work underscores the potential of homogeneous, amorphous MOF-based resists—readily deposited by MLD in thicknesses below 20 nm—to fulfill the requirements for next-generation high-NA, metal-containing EUV (13.5 nm) resist materials. We also provide an initial evaluation of aZnMIm for use in BEUV (6.7 nm) lithography.

We begin by examining the exposure of MLD-deposited aZnMIm resists under an EUV flood source and offer a proof-of-concept demonstration of patterning through liquid development. Next, we present EUV contrast curve data for aZnMIm films developed in the liquid-phase, followed by

https://doi.org/10.1021/acs.chemmater.5c01476
Chem. Mater. 2025, 37, 8548−8567

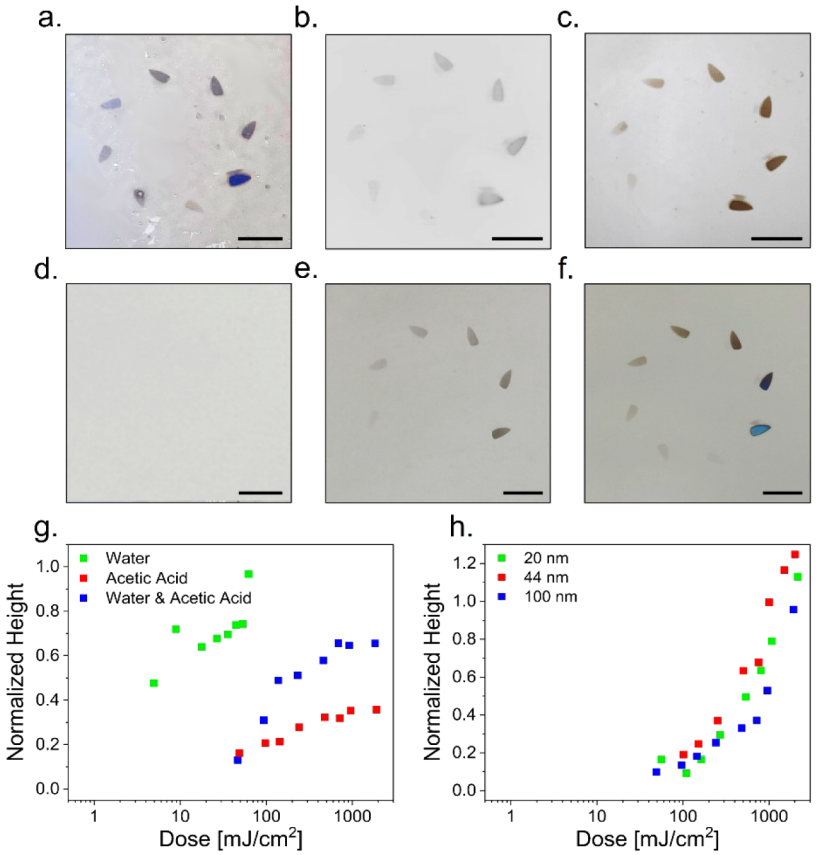

Figure 2. EUV contrast curves of aZnMIm resists. (a) 115 nm thick aZnMIm resist exposed to EUV doses between 5 and 62 mJ/cm^2 and developed in DI water for 10 min. (b) 98 nm thick aZnMIm resist exposed to EUV doses between 49 and 1909 mJ/cm^2 and developed in 655 μM acetic acid for 2.5 min followed by a methanol rinse. (c) 99 nm thick aZnMIm resist exposed to EUV doses between 47 and 1834 mJ/cm^2 and developed in DI water for 5 min, 655 μM acetic acid for 1 min, and rinsed with methanol. (d) 20 nm thick aZnMIm resist exposed to EUV doses between 50 and 1970 mJ/cm^2 and developed using exposure to hfacH vapor at 120 °C for 15 s. The film is too thin to be visible by eye. (e) 44 nm thick aZnMIm resist exposed to EUV doses between 102 and 2009 mJ/cm^2 and developed using exposure to hfacH vapor at 120 °C for 30 s. (f) 100 nm thick aZnMIm resist exposed to EUV doses between 49 and 1917 mJ/cm^2 and developed using exposure to hfacH vapor at 120 °C for 60 s. All scale bars in (a)−(f) are 10 mm. (g) EUV contrast curves of liquid developed aZnMIm resists shown in (a)−(c). (h) EUV contrast curves of vapor developed aZnMIm resists shown in (d)−(f). Heights were measured via spectroscopic ellipsometry and then normalized with respect to the original thickness of the film measured by *ex situ* ellipsometry before EUV exposure. Doses from lowest to highest (starting from the bottom center (6 o'clock position) and progressing clockwise to the highest dose (5 o'clock position)) are listed in Table S1.

results for dry development using hfacH vapor. We then discuss the characterization of aZnMIm films using various experimental techniques—photoelectron spectroscopy (PES), EUV absorption/reflectometry, total electron yield (TEY), residual gas analysis (RGA), and time-of-flight secondary ion mass spectrometry (TOF-SIMS)—to determine the essential properties required to evaluate their chemical response under EUV exposure. These findings are compared with those of other EUV resists of interest. In the concluding section, we assess the potential performance of aZnMIm as a resist for exploratory future BEUV lithography (BEUVL).

RESULTS AND DISCUSSION

EUV Exposure. As stated above, we have previously explored the electron beam behavior of amorphous zinc-imidazolate thin films, demonstrating their viability as high-resolution patternable resists. Because metals generally exhibit higher EUV absorption cross-sections compared to the elements typically used in polymer-based resists, metal-containing aZnMIm formulations present a promising avenue for EUV photoresist design. To test their EUV performance, aZnMIm films were grown on 100 mm Si (100) wafers from the vapor-phase using methods reported in our previous work.[48] In brief, diethyl zinc (DEZ) and 2-methylimidazole (2MIm) were pulsed sequentially into a home-built MLD reactor operating at a temperature of 150 °C. Films with thicknesses between 2 and 200 nm are routinely deposited by controlling the number of MLD cycles.

For the initial experiments, 100 nm thick films were deposited because this thickness gives a visible color appearance, making any subsequent changes in the film thickness readily detectable by visual inspection. Figure 1a shows a 100 mm diameter wafer before (left) and after (right) deposition of 650 cycles of aZnMIm, yielding a smooth (mirror-like), homogeneous deep purple film. The excellent spatial uniformity of the deposited films was measured using *ex situ* ellipsometry and is shown in Figure 1b. While the film thickness is highest closest to the precursor inlet and slightly thinner along the top and bottom edges, the film thickness varies 3.5% or less from the average value across all measured regions of the 100 mm diameter wafer and varies 1% or less from the average value in the central region of the wafer (within ca. 30 mm radius), where it is exposed to EUV light as shown in the schematic given in Figure 1c (EUV exposure was

https://doi.org/10.1021/acs.chemmater.5c01476
Chem. Mater. 2025, 37, 8548−8567

carried out on an experimental general-purpose EUV flood source beamline at EUV Tech Inc. in Martinez, California). 100 mm Si wafers coated with 15−100 nm of aZnMIm were loaded vertically into a high-vacuum chamber and pumped down. The EUV source was started, and a diode was inserted between the sample and the beam to measure the beam current (shown schematically in Figure S1). After the current was recorded, the diode was removed, and a recipe was loaded. The wafer was rotated to 0°, and the shutter was opened, exposing each spot for the desired amount of time before rotating to the next preset angle. After all locations were exposed, the diode was inserted and the beam current was recorded again. The beam was shut off, and the system was vented. After being vented, the wafer was removed from the chamber. Following exposure, the photoresist was developed in an appropriate solvent or vapor to reveal the EUV exposure spots. Using this method, many different doses were tested at once to benchmark photoresist sensitivity and contrast in various developers. These results will be reported in a later section of this paper.

While EUV flood sources are primarily used for large-area irradiation, it is also possible to fabricate test patterns with a flood tool by using a proximity transmission photomask. A small-scale experimental transmission photomask was fabricated by Applied Nanotools Inc. (ANT) for testing on the EUV flood source beamline at EUV Tech Inc. and is shown schematically in Figure 1d. This photomask was taped to the resist-coated wafer, in line with the beam (Figure S2). The mask, shown in Figure 1e, is a 5 × 5 mm silicon chip frame with a ∼1.1 × 1.1 mm cutout, a 100 nm thick SiC support membrane, and a 200 nm thick electroplated gold (Au) film patterned with EBL to produce grating patterns of various dimensions. The mask has four grating sizes, 1, 2, 5, and 10 μm, with pitches of 2, 4, 10, and 20 μm, respectively. When EUV light is exposed through the mask, photons pass through the SiC membrane at a transmittance of approximately 64% (Figure S3). EUV photons are absorbed by the Au gratings on top of the SiC membrane, which transmit less than 0.005% of the 92 eV photons (Figure S4). Thus, the EUV light that reaches the photoresist passes through the photomask only from areas without the Au gratings. Using this process, proof-of-concept test structures using a 102 nm thick aZnMIm photoresist were fabricated using solvent-based methodology (consisting of immersion in DI water for 5 min and then in 655 μM acetic acid for 2 min; the rationale for water and acetic acid development is discussed in the next section of this paper and is shown in Figure 2a−c) to produce 10 μm wide, 20 μm pitch line patterns (Figure 1f). Considering the transmission of the SiC membrane, the line patterns were exposed to a dose of approximately 293 mJ/cm^2. Test structures patterned at doses as low as 120 mJ/cm^2 are provided in Figure S5. Based on these test patterns, it was demonstrated for the first time that aZnMIm resists, which have previously shown capability as high-resolution electron beam resists, can also function as EUV-sensitive negative-tone photoresists. Therefore, future experiments designed for high-resolution patterning should be pursued. However, this capability is not available to us at this time. In what follows, we provide an assessment of the EUV response and fundamental properties of these promising materials in preparation for high-resolution experiments.

Solvents for Residue-Free Liquid-Phase Development. To realize the potential of aZnMIm thin films as EUV photoresists, their lithographic properties were investigated by using the EUV flood exposure tool described in Figure 1c. aZnMIm films ca. 100 nm thick were deposited on silicon wafers and exposed to EUV photons at various doses to benchmark EUV sensitivity. Water has been used as an effective developer for negative-tone ZIF-type materials in the past[43,44] and was thus selected to benchmark EUV sensitivity relative to known EBL performance. A 115 nm thick aZnMIm resist exposed to EUV doses between 5 and 62 mJ/cm^2 and developed in DI water with gentle agitation for 10 min is shown in Figure 2a. EUV spots were retained even at the lowest exposure dose (5 mJ/cm^2), showing impressive sensitivity when developing in water. However, a significant amount of material was also observed in the nonirradiated areas in addition to uneven development, significant sample-to-sample variation, delamination, and peeling of the remaining material even when gently agitating the development solution (Figure S6a).

Dissolution of as-deposited films in water was further investigated (Figure S6b) and revealed two distinct regimes of dissolution behavior. In the first 3 min of immersion in water, aZnMIm undergoes a rapid dissolution burst that reduces the film thickness from about 100 to around 30 nm. After this initial rapid dissolution phase, the remaining material dissolves much more slowly, requiring tens of minutes to hours for complete removal, depending on the original film thickness. While the aforementioned development took place in a batch process where the films were immersed in water while gently agitating the beaker, development was also performed under both flowing solvent and spin-off dissolution (Figure S6c) to evaluate the effect of replenishing the dissolution front with fresh water. Flowing water over the film surface at a rate of 2 mL/min as well as spin-off dissolution where the wafer was spun at a rate of 2000 rpm reveals two regimes of dissolution consistent with batch processing (rapid burst of dissolution followed by slow dissolution). Spin-off dissolution, however, is capable of removing a 100 nm thick aZnMIm film completely in 15 min compared to hours for batch and flow dissolution. This discrepancy is most likely attributed to the behavior of spin-off dissolution, which rapidly replenishes solvent to the film surface, whereby solvent droplets rapidly spread across the wafer surface on the millisecond time scale,[66] efficiently displacing the saturated solution and supplying fresh solvent to the film interface, thus persistently perturbing the diffusion boundary layer and facilitating enhanced mass transport of dissolved species. This results in the acceleration of the slower second dissolution phase for spin-off compared with batch and flow development. Regardless, dissolution of aZnMIm in water by all methods results in a two-stage dissolution behavior, likely as a result of rapid changes in pH near the film-water interface.

Calculations detailing 2MIm and Zn speciation based on pH dependence were performed and are included in Section S1. aZnMIm film dissolution rates exhibit a strong pH dependence likely due to 2MIm preferentially dissolving from the film, causing a rise in 2MIm concentration in the solution and an increase in pH as shown in Figure S6d. This is anticipated by earlier studies demonstrating pH changes during the dissolution of the crystalline Zn-2MIm framework, ZIF-8.[70] We hypothesize that as the local pH of the water solution increases due to the dissolution of 2MIm, the dissolution rate of Zn in the film decreases. We base this hypothesis on Zn speciation dependence on pH[71] and the pH changes caused by 2MIm dissolution. Based on its pK_a value, the dissolution of

https://doi.org/10.1021/acs.chemmater.5c01476
Chem. Mater. 2025, 37, 8548−8567

2MIm in water causes the pH to increase to nearly 11 (Figure S6d). This increase, which will happen at a boundary layer near the dissolving surface, causes Zn speciation to shift so that its dominant component is the least soluble species ($Zn(OH)_2$) (Figure S6e).[71] At this high local pH, the initially dissolved Zn redeposits and/or the remaining Zn does not dissolve, while imidazole can keep dissolving. This hypothesis is supported by X-ray Photoelectron Spectroscopy (XPS) analysis of the material remaining after immersion of aZnMIm in water for 8 min, as shown in Figure S7a. Compared to the as-deposited aZnMIm spectrum, the film remaining after the rapid dissolution step exhibits a decrease in the C 1s signal, a near-complete loss of the N 1s signal, an increase in the intensity of the O 1s signal, and the maintenance of the Zn 2p signal. The high-resolution XPS data in Figure S7b−e suggest that the dissolution of aZnMIm in water proceeds through the preferential removal of 2MIm (as evidenced by the loss of the N 1s signal from the 2MIm linker) and the retention of a $Zn(OH)_x$-rich material, shown by the potential Zn−O peak at 531.7 eV[72] in the O 1s region. This is further supported by the hypothesis that Zn- and 2MIm-containing ZIF-L produces zinc oxo- and hydroxo-type compounds when partially dissolved in pure water.[73]

As an alternative to pure water, dilute acetic acid in water was explored as a potential developer for aZnMIm as ZIF-8 is prone to decomposition in acidic aqueous environments,[74−76] and acetic acid has been successfully used as a developer for various metal−organic resists including zinc-oxo cluster resists,[77] cobalt-based resists,[78] bismuth oligomer dichloride resists,[79] and zirconium-containing resists.[80] The dissolution behavior of as-deposited aZnMIm films was tested in three different concentrations of aqueous acetic acid solutions: 0.2 M (pH ∼ 2.7), 655 μM (pH ∼ 4), and 15.5 μM (pH ∼ 5) (Figure S8). In 0.2 M acetic acid, the films dissolved at a rate >2 nm/s, while in 15.5 μM acetic acid, the films dissolved at a considerably slower rate; a 22 nm thick film could not be removed within 5 min. The intermediate concentration, 655 μM acetic acid, exhibited a linear dissolution rate and resulted in the removal of the as-deposited film on a reasonable development time scale (less than 60 s for a 22 nm thick film). This leads to the conclusion that the initial pH of the solution was low enough that upon imidazolate ion dissolution and protonation, the local pH did not increase enough to considerably slow down the dissolution rate. Although further optimization may be possible, 655 μM acetic acid was selected for testing to see if irradiated areas could be selectively retained. 22 nm thick aZnMIm films were deposited on Si substrates and exposed to electrons with an energy of 5 keV at various doses and subsequently developed with 655 μM acetic acid for 60 s followed by rinsing with methanol to generate the dose matrix test patterns shown in Figure S9. Complete removal of material in nonexposed areas and good resistance of the irradiated areas were observed at doses similar to ZIF-L EBL sensitivity with water development.[44]

Encouraged by the above EBL results, 100 nm thick aZnMIm resists were exposed to EUV doses between approximately 50 and 2000 mJ/cm^2 and developed in 655 μM acetic acid for 1.5 to 3 min (Figure S10). With considerably thicker films, a longer development time was required, and development times between 1.5 and 2.5 min did not show complete removal of material in the areas that were not exposed to EUV. A 98 nm thick aZnMIm film exposed to EUV doses between 49 and 1909 mJ/cm^2 and developed in 655 μM acetic acid for 2.5 min followed by a methanol rinse is shown as Figure 2b. Progression of development from 2.5 to 3 min shows removal of both irradiated and nonirradiated areas, with nearly all of both areas being removed by 3 min even at extremely high doses (>500 mJ/cm^2). XPS of a wafer developed in 655 μM acetic acid for 3 min (Figure S7a) shows a clean wafer with a survey spectrum nearly identical to a bare silicon wafer, indicating complete removal of nonexposed areas. The visible contrast and height retention in the exposed areas are very poor in acetic acid, as the differences in the rate of dissolution of the irradiated vs nonirradiated areas are small after the initial onset of development. This effect has previously been observed with other Zn-containing resists developed in acetic acid, resulting in poor contrast due to partial dissolution of exposed areas.[77] For better lithographic results, a more selective developer is required.

aZnMIm development in water works well to dissolve a significant amount of the resist at low doses but leaves nearly 30 nm of material in the nonexposed regions for a 100 nm thick resist, and acetic acid development removes both regions rapidly. Based on these findings, an alternative development method was attempted. EUV-exposed aZnMIm resists were developed first in water to remove a significant amount of material and then placed into 655 μM acetic acid for 60 s to remove the remaining unremoved material in the nonexposed regions. This development process, given in Figure 2c, demonstrates near-complete removal (native oxide thickness in all nonexposed areas except the wafer center) of all material from the nonexposed regions while retaining appreciable thickness in the EUV-treated areas. Figure S11 shows spatially resolved ellipsometry of an EUV spot exposed to a dose of 460 mJ/cm^2 on the wafer in Figure 2c. Measurements obtained around the EUV exposure spot show a steep drop to the native oxide thickness next to the spot. Except at the wafer center where a 6 nm film remains, the remaining nonexposed wafer shows complete removal of aZnMIm after development using the combination of water followed by acetic acid, in agreement with the XPS data shown in Figure S7a. Other liquid development approaches, including the use of basic and organic solvents, are possible and will be the subject of future work. Figure S12a-b demonstrates the potential of using both tetramethylammonium hydroxide (TMAH) (0.265 and 0.55 M) and methanol as negative-tone developers for aZnMIm. Solvents such as PGME, EGMEA, PGMEA, *n*-butyl acetate, and anisole have shown efficacy as developers for other Zn-based photoresists[81] and will be investigated in the future.

Vapor-Phase Development. Figure 2d−f shows images from films developed using our previously introduced method based on the β-diketone etchant, hfacH.[48] A 20 nm thick aZnMIm resist exposed to EUV doses between 50 and 1970 mJ/cm^2 and developed using exposure to hfacH vapor for 15 s in a 120 °C oven is shown in Figure 2d; this film is too thin to be visible by eye. Figure 2e is from a 44 nm thick aZnMIm resist exposed to EUV doses between 102 and 2009 mJ/cm^2 and developed using exposure to hfacH vapor for 30 s. It demonstrates an all-dry aZnMIm EUV resist for the first time, showing a clear contrast and retention of the EUV-treated regions. A 100 nm thick aZnMIm resist exposed to EUV doses between 49 and 1917 mJ/cm^2 and developed using exposure to hfacH vapor for 60 s is also given as Figure 2f, with film remaining even at the lowest tested dose of 49 mJ/cm^2.

https://doi.org/10.1021/acs.chemmater.5c01476
Chem. Mater. 2025, 37, 8548−8567

Contrast Curves. Heights of the liquid-developed EUV exposure spots from Figure 2a–c were measured using spectroscopic ellipsometry and plotted vs EUV dose to create the contrast curves shown in Figure 2g. The EUV dose per square centimeter was calculated using the EUV exposure time, beam size, and photodiode current being measured in the tool. aZnMIm sensitivity, defined as the dose required to retain 50% of the normalized thickness, was calculated to be 5 and 181 mJ/cm^2 for development in pure water and development in water, followed by 655 μM acetic acid, respectively. Development in only 655 μM acetic acid resulted in generally poor sensitivity with a contrast curve that leveled off around a normalized thickness of 0.35, ultimately not allowing for the calculation of a specific sensitivity value. The contrast curves in Figure 2g demonstrate that aZnMIm EUV sensitivity is dramatically impacted based on the choice of developer; water development gives very high sensitivity but poor overall development while acetic acid gives a much lower sensitivity resist and partial removal of exposed areas but with complete removal of nonexposed material. The combination method of immersion of aZnMIm in water and then acetic acid gives intermediate EUV sensitivity and residue-free development. The EUV sensitivity for liquid-developed aZnMIm with water followed by acetic acid is worse than other negative-tone metal-containing resists such as Zn-containing MOF-inspired EUV resists which have a sensitivity of approximately 12 mJ/cm^2,[19] indium nitrate hydrate resists with a sensitivity of 21 mJ/cm^2,[25] or the dihydroxide form of a tin-oxo cluster with a sensitivity of approximately 25 mJ/cm^2.[30] Because the sensitivity of aZnMIm resists varies greatly as a result of processing conditions, further optimization of the development process has the potential to identify a solvent that improves sensitivity into a desirable range with residue-free development.

Lithographic contrast (γ), or the ability of a photoresist to differentiate between the properties of irradiated and nonirradiated areas, is essentially the slope of the contrast curve and can be calculated using D_{100}, the lowest electron dose at which the original resist thickness is retained, and D_0, the maximum electron dose for which the resist thickness equals zero. The aZnMIm EUV contrast was estimated as 0.56, 0.30, and 0.51 for development in pure water, 655 μM acetic acid, and water, followed by 655 μM acetic acid, respectively. The combination of water and acetic acid shows an intermediate lithographic contrast between the two individual developers. All developers, especially acetic acid, lead to poor contrast with aZnMIm resists, with a gradual increase in remaining thickness with increasing EUV dose, likely due to the high solubility of both the exposed and nonexposed areas in each solvent. These values are similar to Zn(MA)(TFA) resists developed in acetylacetone (γ = 0.63) and acetic acid (γ = 0.45)[77] but fall short of the industrially viable range (approximately >2).

Contrast curves for three different aZnMIm film thicknesses exposed to EUV and developed by hfacH vapor at 120 °C are plotted in Figure 2h. The behavior of all three films is quite similar, yielding overlapping curves that do not level off to give the classic sigmoidal contrast curve behavior. Instead, the measured height continues to increase with the dose, ultimately resulting in poor lithographic performance for all three films. Under these conditions, aZnMIm exhibits sensitivities of 547, 375, and 915 mJ/cm^2 for 20, 44, and 100 nm thick aZnMIm resists, respectively. The two thinner samples demonstrate sensitivities on the same order of magnitude, comparable to a suite of tin carboxylate-type resists with doses to size in the range of 300 to 600 mJ/cm^2,[29] or to negative-tone platinum and palladium carbonate resists of type $L_2M(CO_3)$ using doses between 282 and 733 mJ/cm^2.[82] The increased dose required for the 100 nm thick aZnMIm resist could be due to the increased thickness. The low sensitivity of vapor-developed resists can be attributed to the high dose required to chemically alter aZnMIm sufficiently to prevent hfacH diffusion into the material. This result was anticipated based on the high onset dose required to retain electron beam-exposed aZnMIm after it had been converted to a more dense, nonvolatile matrix with degraded imidazole ligands.[48]

The lithographic contrast of the vapor-developed aZnMIm films was also calculated. To maintain consistency, the maximum dose was used as D_{100} for each film as leveling off of the contrast curve was not observed. The vapor-developed contrast values were estimated as 0.49, 0.50, and 0.50 for the 20, 44, and 100 nm thick aZnMIm films, with all values being nearly the same, owing to their similar processing conditions, although more data points at both lower and higher doses are needed to give a more accurate contrast estimate. Similar to the dry development of aZnMIm resists, Kenane et al. found that Lam Research's all-dry resist deposition and development process results in a contrast curve with a near-linear response to an increase in EUV dose and a lithographic contrast of 0.53.[83] They hypothesize that reacting their EUV-exposed tin-oxo cluster-based resist ($(RSn)_xO_yH_z$) with gaseous HBr results in sequential molecular cleavage of Sn–O–Sn bonds, allowing for progressive development that results in more linear contrast behavior that still allows for the patterning of high-resolution dense features. While the chemistry of all-dry-deposited and developed aZnMIm resists is different, sequential molecular-scale removal of the resist rather than conventional solubility-driven development could provide a potential explanation for the linear behavior and low contrast observed in Figure 2h. It may, therefore, be anticipated that aZnMIm could also exhibit high-resolution performance. In support of this hypothesis, very high-resolution dense features (16 nm lined features with 20 nm pitch) were achieved for all-dry aZnMIm resists patterned by EBL despite a low contrast (γ = 1.59).[67]

EUV Response Characteristics of aZnMIm Resists. Motivated by the potential of aZnMIm as an EUV photoresist established above, we explored its EUV response characteristics to advance the fundamental understanding of its interaction with EUV photons and explain the observed experimental phenomena. During EUV exposure, a small fraction, typically between 10% and 30%, of 92 eV photons will be absorbed by a 30 nm thick resist.[84,85] After photoabsorption, a primary photoelectron generated in either the resist or underlayer will generate a cascade of low-energy secondary electrons (LESEs) by inelastic scattering. The LESEs are ultimately responsible for the chemical changes within a photoresist leading to dissolution/etching contrast during resist development.[4−6] Given the vital role that LESEs play in photopatterning, it is essential to understand both how efficiently a material absorbs EUV photons and how it subsequently generates electrons. PES can be used to investigate these essential resist properties, as it provides insights into both the abundance of emitted electrons and their energy distribution. By characterizing the energy spectrum of EUV-generated electrons, PES can aid in understanding the

https://doi.org/10.1021/acs.chemmater.5c01476
Chem. Mater. 2025, 37, 8548−8567

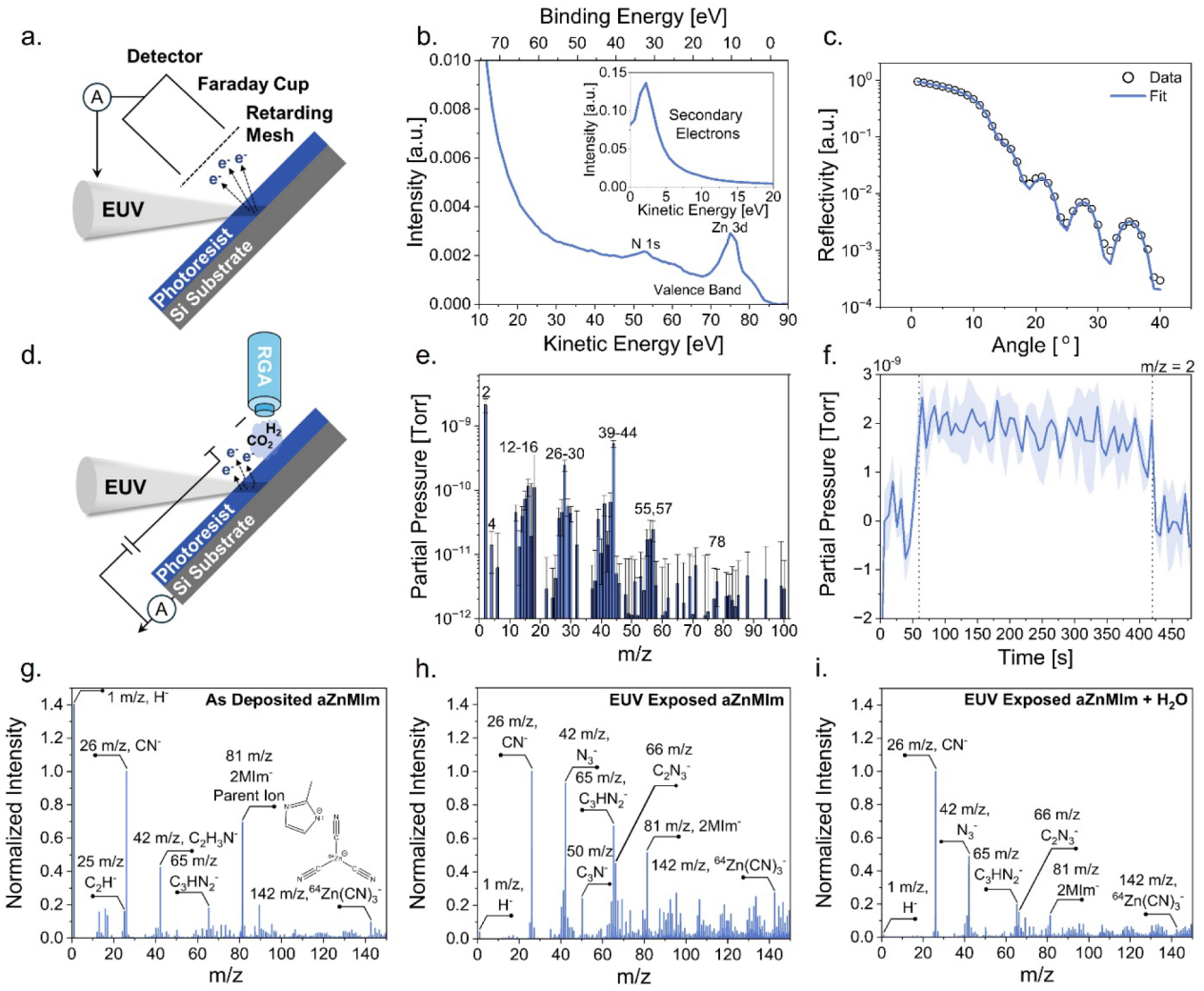

Figure 3. EUV characterization of aZnMIm films. (a) Schematic for the EUV PES experimental setup in (b). (b) EUV photoelectron spectrum of an aZnMIm film showing the distribution of primary and secondary electrons. The inset shows a zoomed-in view of the low-energy secondary electrons (<20 eV). (c) Reflectometry data obtained experimentally and model fit for a 50 nm thick aZnMIm film to determine EUV absorption. (d) Experimental schematic for RGA shown in (e) and (f). (e) Representative outgassing spectrum of an aZnMIm photoresist with dominant ion signals labeled. (f) Ion signal over time for the most prominent outgassing signal, m/z = 2. (g) TOF-SIMS mass spectrum of a 32 nm thick as-deposited aZnMIm film. (h) TOF-SIMS mass spectrum acquired for a 100 nm thick aZnMIm film exposed to EUV light at EUV Tech Inc. using a dose of 4036 mJ/cm^2. (i) TOF-SIMS mass spectrum of a 100 nm thick aZnMIm film exposed to EUV light at EUV Tech Inc. with a dose of 4036 mJ/cm^2 and then developed in water for 15 min. The mass spectra in (g)−(i) were normalized with respect to the signal intensity at m/z = 26.

mechanisms that govern metal−organic resist performance. However, while PES can probe electron emission, it does not directly address EUV absorption efficiency, which is equally crucial for EUV resist performance.

In our previous study, we investigated aZnMIm films in the context of EBL,[48,60,67] which is often used as a probe for EUV performance as LESEs drive the chemical reactions that allow pattern development in both cases.[4−6] While EBL is a useful tool for preliminary screening of EUV resists[86,87] and is often completed first to prove viability for EUV testing,[19,33,88−92] EUV and EB performance metrics do not always correlate.[93−95] This is a consequence of the fact that the efficient use of EUV light is a crucial photoresist property, and EBL, even if one assumes it to be a perfect mimic for EUV secondary electron generation, provides no information about the ability of a resist to absorb EUV light. Therefore, EUV reflectometry and absorption measurements are necessary to directly evaluate how effectively a material absorbs EUV photons. Complementary to reflectometry, TEY measurements provide additional insight into the EUV absorption process by quantifying the number of electrons able to escape from a resist after photon absorption. TEY is directly proportional to the number of electrons generated within a resist during EUV exposure, making it a valuable metric for assessing resist efficiency and explaining trends observed in reflectometry experiments.

Aside from EUV absorption and LESE generation, a thorough understanding of the chemistry initiated during exposure is required for optimizing photoresist performance, controlling patterning outcomes, minimizing defects, and ensuring compatibility with industrial processes. It is particularly important that all generated molecules, especially gaseous ones, comply with fabrication laboratory restrictions and are compatible with expensive lithography equipment. Controlling and minimizing photoresist outgassing—or the release of volatile compounds such as residual solvent, reaction

https://doi.org/10.1021/acs.chemmater.5c01476
Chem. Mater. 2025, 37, 8548−8567

byproducts, or components of the resist formulation itself[96] during EUV exposure—are critical because of the potential impact on both the lithography process and contamination of EUV equipment.[97−99] EUV instruments use reflective optics, such as multilayer mirrors, which are highly sensitive to contamination.[100] Even a small amount of deposited outgassed material on these mirrors can reduce their reflectivity, thereby decreasing the intensity of EUV light reaching the wafer and ultimately lowering wafer throughput.[101−103] Additionally, EUV instruments operate in a high-vacuum environment to maintain a fully reflective optical path and prevent EUV absorption by molecules other than those in the photomasks or resists.[104] Outgassing of molecules from the resist can not only disrupt this vacuum but also cause an increase in the partial pressure of gases in the exposure chamber.[102] This process variability can affect the consistency of the lithography process and potentially lead to pattern defects due to the redeposition of volatile compounds on the resist surface. To address this challenge, RGA tools are commonly employed for systematic outgas evaluation under controlled conditions.[96,105]

While the aforementioned techniques provide important insights into EUV exposure mechanisms, they do not directly reveal the chemical modifications within the resist induced by EUV exposure. To address this limitation, we can use TOF-SIMS to probe the molecular-level changes occurring before and after EUV exposure. By comparison of the TOF-SIMS spectra of aZnMIm films before and after EUV exposure, bond cleavages, molecular fragmentation, and the formation of chemical species resulting from EUV photoreactions can be inferred. Additionally, by comparison of TOF-SIMS before and after EUV exposure, a loss of signal attributed to volatile molecules lost via outgassing can be detected to complement RGA studies. By integration of TOF-SIMS analysis with PES, EUV reflectometry, TEY, and RGA, a comprehensive understanding of how aZnMIm resists interact with EUV photons can be developed. Here, we provide the first comprehensive evaluation of amorphous zeolitic imidazolate resists using these complementary techniques.

EUV Photoelectron Spectroscopy. EUV PES was performed on an ∼25 nm thick aZnMIm film using the experimental setup indicated in Figure 3a at the Advanced Light Source (ALS) at Lawrence Berkeley National Laboratory, beamline 12.0.1. The sample was exposed to EUV photons, and the electrons emitted by the sample were collected by a retarding field analyzer. A negative retarding potential was applied to the fine metal mesh mounted in front of the Faraday cup to ensure that electrons with kinetic energy less than the applied voltage are not transmitted through the mesh. Electrons with kinetic energies larger than the applied voltage are transmitted through the mesh, and after being accelerated by a + 5 V bias applied to the Faraday cup, they generate the measured current (intensity). The derivative of the measured signal represents PES.

In EUV PES, high kinetic energy (KE) signals (>60 eV) in many cases originate due to emission of primary valence electrons (photoelectrons) after the absorption of EUV photons. These primary electrons with high KE will likely undergo inelastic scattering events within the photoresist, losing part of their KE with each collision and leading to the emission of secondary electrons with low KE. The cascade of such events will lead to almost complete loss of KE by a primary electron and the emission of several low KE secondary electrons. This process is evident in the photoelectron spectrum of aZnMIm given in Figure 3b. Above 20 eV, a small feature appears at 52.6 eV and a sharp peak emerges at 75.0 eV, after which the signal drops to zero around 85.4 eV. At low KE, the signal intensity increases sharply due to the generation of multiple LESEs from each photoelectron, resulting in a broad high-intensity peak at 2.2 eV (also shown as an inset). However, at very low KE, the signal intensity falls off because electrons with such low energy cannot escape the sample, owing to the potential barrier at the film-vacuum interface. To analyze key features present in the photoelectron spectrum, it is typical in solid-state PES to relate KE to literature binding energy (BE) values by subtracting the KE from the Fermi energy (FE).[85] The FE, which can be estimated as the signal onset in the photoelectron spectrum, was found to be 85.4 eV (Figure 3b). The sharp peak in the aZnMIm photoelectron spectrum at a KE of 75 eV can be attributed to Zn 3*d* electrons and yields an experimentally observed BE relative to the FE of 10.4 eV. This BE correlates with the literature value for the Zn 3*d* doublet peak (10.2 eV for Zn $3d^{3/2}$ and 10.1 eV for Zn $3d^{5/2}$).[106] A small peak at a KE of 52.6 eV, corresponding to an experimentally observed binding energy of 32.8 eV, could be due to the emission of semicore N 2*s* electrons, which exhibit a reported electron BE of 37.3 eV.[106]

From the raw data, it is possible to determine the ratio of slow electrons (<20 eV, LESEs) to fast electrons (20−95 eV) using the difference in signal intensity at retarding potentials of 0 and 20 V for the quantity of slow electrons and 20 and 95 V for fast electrons, respectively. For a 10 nm thick aZnMIm film, the total electron signal (encompassing 0−95 eV) was calculated as 0.825, with 0.693 coming from slow electrons and 0.132 from fast electrons. This translates to 84% slow and 16% fast electrons, yielding an overall slow-to-fast ratio of 5.27. When compared with poly(4-hydroxystyrene) (PHS), a stable reference polymer resist, aZnMIm exhibits stronger emission of both primary and secondary electrons, as reflected by PHS's lower total signal of 0.631 (with a slow electron contribution of 0.549 and a fast electron contribution of 0.081) (Figure S13). Nevertheless, PHS has a higher slow-to-fast electron ratio of 6.76, suggesting that it produces slow electrons more efficiently relative to its primary electron emission than aZnMIm. For comparison, industry-standard metal-containing tin-oxo-type resists show a significantly increased yield of fast electrons from the high EUV absorption of Sn atoms but only a slightly increased slow electron yield resulting in a slow-to-fast electron ratio of 7.20.[107]

EUV Reflectometry. EUV absorption measurements were performed at the Advanced Light Source (ALS) beamline 6.3.2 using the reflectivity method where the reflectivity of an aZnMIm resist at a wavelength of 13.5 nm was measured as a function of angle and plotted in Figure 3c. The experimental data were fitted using methods described elsewhere[108,109] and show good agreement between calculations and experimental results. From the fit, the dispersive and absorptive components of the film refractive index, δ and β, were obtained and found to be 0.0220 and 0.0067, respectively. Using the absorptive component of the refractive index, the linear attenuation coefficient (μ), also known as the EUV absorption coefficient, can be determined using eq 1:

$$\mu = \frac{4\pi\beta}{\lambda} = \frac{\rho N_A \sigma}{M} \quad (1)$$

https://doi.org/10.1021/acs.chemmater.5c01476
Chem. Mater. 2025, 37, 8548−8567

where λ is the irradiation wavelength, ρ is the film density, N_A is Avogadro's constant, M is the molar mass, and σ is the photoabsorption cross-section. aZnMIm resists have an experimentally determined EUV absorption coefficient of 6.2 μm^{-1}. In comparison, typical polymer-based CARs have absorption coefficients in the range of 4.8 μm^{-1}, common resists poly(methyl methacrylate) (PMMA) and PHS have measured coefficients of 5.5 and 3.9 μm^{-1}, respectively, and tin-oxo cages/clusters have absorption coefficients on the order of 10−20 μm^{-1} depending on the choice of counterion used.[108,110,111] Zirconium-oxo cluster-based resists show similar EUV absorption coefficients as aZnMIm resists, on the order of 6−7 μm^{-1}.[111]

Once the linear attenuation coefficient is determined, the right side of eq 1 can be rearranged and expanded to form eq 2 to solve for film density:

$$\rho = \frac{\mu \sum_i x_i A_i}{N_A \sum_i x_i \sigma_{ai}} \quad (2)$$

where x_i is the atomic fraction of each element and A_i is the atomic weight of element i. Using the experimental atomic photoabsorption cross-sections calculated from the atomic scattering factors listed in the CXRO X-ray database (σ_{Zn}: 4.74 × 10^6 cm^2/mol, σ_C: 3.51 × 10^5 cm^2/mol, σ_N: 7.30 × 10^5 cm^2/mol, σ_H: 1.51 ×10^4 cm^2/mol),[106] the density of aZnMIm films was calculated as 1.39 g/cm^3, which is higher than PMMA (1.18 g/cm^3) but lower than tin-oxo-type materials (1.84 g/cm^3).[6] Crystalline ZIF-8 has a density of 0.98 g/cm^3, while amorphous ZIF-8 films made by spin-coating have a density of 1.62 g/cm^3.[66] Density calculations and parameters are included in Section S2. EUV reflectometry analysis of polymer resist materials has shown that more dense resists tend to have higher absorption coefficients than less dense films of the same stoichiometric ratio, as is the case with PMMA and poly(4-methoxystyrene).[108]

Total Electron Yield (TEY). During EUV exposure, a 12 V bias was applied to draw away all escaped electrons, and the drain current was measured at low and high flux. The measured drain current was normalized by the photon flux, which was measured with a silicon photodiode. The resulting TEY was determined as the electron yield per unit of photon flux. Using the low flux data, the TEY for a 10 nm thick aZnMIm film was found to be 11.48 × 10^{-4} a.u., which is nearly the same as the TEY of PMMA, found experimentally to be 11.49 × 10^{-4} a.u.[112] The TEY of aZnMIm is higher than most styrene-based resists (polystyrene: 6.15 × 10^{-4} a.u., poly(4-hydroxystyrene): 7.06 × 10^{-4} a.u., and poly(4-cyanostyrene): 9.94 × 10^{-4} a.u.) other than poly(pentafluorostyrene), which has a TEY of 15.42 × 10^{-4} a.u.[112]

Interestingly, the TEY of the aZnMIm film is similar to that of PMMA, despite the two materials having different EUV absorption coefficients (6.2 μm^{-1} for aZnMIm vs 5.5 μm^{-1} for PMMA). A previous study has shown a correlation between TEY and the EUV absorption coefficient, with TEY being proportional to the product of the EUV absorption coefficient, quantum efficiency (electrons produced per absorbed photon), and the electron attenuation length (EAL).[112] The EAL, defined as the resist distance required to reduce the number of emitted secondary electrons by a factor of 1/e (initial secondary electron population decreases to ∼37%), provides insight into the distance that slow electrons can travel within a material and is directly related to feature blur and photoresist resolution. Several techniques have been used to measure EAL including low-energy electron transmission,[113,114] reflection energy loss spectroscopy,[115] low-energy electron beam exposure,[116] and Monte Carlo simulations/inelastic mean free path (IMFP) calculations.[117] While these methods can probe electron penetration depths, they are often unable to capture slow electron (<20 eV) behavior and may neglect elastic scattering effects, leading to an underestimation of EAL by up to 30% for IMFP calculations.[117] Other studies have directly measured EAL experimentally using the substrate overlayer[118,119] method for a number of organic-based photoresists,[112,120,121] with some resolving the EAL as a function of kinetic energy,[121,122] revealing relatively stable EAL values between 10 and 90 eV. Because EUV photoresists produce a large fraction of secondary electrons with energies below 90 eV, and in the case of aZnMIm, many below 5 eV, the approach by Kostko et al., which assumes the use of secondary electron energies below 20 eV, is particularly relevant.[112] Using this technique, an EAL of 2.15 nm for PMMA was reported.[112] A different study by Frederick et al. estimated the EAL of a hafnium-based EUV resist as 0.3 nm for 100 eV electrons,[123] though this approach relied on the universal electron attenuation curve[124] which is only valid for the energy range 100 to 30 000 eV and thus does not capture slow electron behavior. Assuming that PMMA and aZnMIm have the same quantum efficiency, the EAL of aZnMIm can be estimated using the established correlation between TEY, EUV absorption coefficient, and EAL.[112] Using the measured TEY of 11.48 × 10^{-4} a.u., the aZnMIm EAL can be estimated as 1.66 nm. Therefore, the TEYs of aZnMIm and PMMA may be the same despite aZnMIm having a higher EUV absorption coefficient because aZnMIm appears to have a shorter EAL. The EAL of aZnMIm could be reduced due to higher material density, electron trapping properties, or a combination of both factors. While quantum efficiency was assumed to be the same for simplicity, differences in the electron yield per absorbed photon could also contribute to the observed TEY similarity between the two materials. Future work will aim to experimentally obtain an EAL value for aZnMIm, considering that previous work on EUV photoresist EAL values has primarily focused on organic-based materials.

Residual Gas Analysis. A schematic of the photoresist outgassing experiment is shown in Figure 3d. After a baseline pressure was collected without EUV exposure, the outgassing signal was measured using an RGA from Stanford Research Systems Inc., capable of detecting mass-to-charge ratios (m/z) ranging from 1 to 300. During the measurement, the shutter blocking EUV light was opened after 60 s, subsequently exposing the photoresist. After approximately 6 min, the shutter was closed. During exposure, m/z from 1 to 200 were repeatedly scanned with each scan taking approximately 6.6 s, tracking the partial pressure increase caused by EUV exposure. Exposure durations correlate with an accumulated dose of approximately 1.3 mJ/cm^2/s. The resulting outgassing mass spectrum was baseline-corrected by subtracting the background signals and the signal from a bare Si wafer (Figure S14). The outgassing signal for each m/z, averaged over the first 20 s after the shutter is open and the sample is exposed, was then used to generate the outgassing spectrum shown as Figure 3e, which gives an overview of the volatile species released during EUV exposure. Peaks with error bars larger than the signal height were neglected as nonreproducible and

https://doi.org/10.1021/acs.chemmater.5c01476
Chem. Mater. 2025, 37, 8548−8567

only peaks with signals larger than the standard deviation were labeled.

The most dominant signal appears at m/z = 2, with other significant peaks occurring at m/z = 4, 12−16, 26−30, 39−44, 55, 57, and 78. While data were collected for m/z = 1−200, only m/z = 1−100 are plotted in Figure 3e as there is no significant outgassing above m/z = 100 aside from m/z = 156 (Figure S15). Outgassing from aZnMIm films can be attributed primarily to H_2 (m/z = 2) and 2MIm (m/z = 12−15, 26−30, 39−44, 55). Interestingly, the largest 2MIm fragments, m/z = 54, 81, and 82, are not present in the aZnMIm outgassing spectrum. Other visible signals may be attributed to common vacuum system contaminants, including CO_2 (m/z = 12, 16, 28, 44), N_2 (m/z = 14, 28), and various hydrocarbons.

To better evaluate individual m/z, isolated ion signals were also baseline-corrected and then plotted against time. The isolated ion signal for m/z = 2, which corresponds to H_2, is plotted as Figure 3f. The hydrogen signal is over an order of magnitude stronger than any of the other outgassing signals (Figure S16). When the shutter opens after 60 s, there is a considerable increase in the ion signal strength upon sample exposure to EUV photons. Over the course of exposure, there is no significant decay in signal strength, dipping only slightly toward the end of the exposure time. This reveals a continuous loss of hydrogen over the entire EUV exposure period. Isolated ion signals for all other significant peaks are included in Figure S16. For most of the isolated signals, as with hydrogen, there is no or a very slow decrease in the outgassing signal with increasing dose. For m/z = 44, which is attributed to CO_2, there is strong outgassing and a sharp signal decay after the first 60 s of exposure, indicating the loss of CO_2 from the resist surface.

TOF-SIMS. A comparison of the TOF-SIMS data acquired from as-deposited and EUV-exposed aZnMIm is presented in Figure 3g−i and reveals that the composition of aZnMIm is significantly altered by EUV exposure. Prior to exposure, the film is known to be composed of Zn(II) ions and 2MIm (anionic) linkers, which is reflected in the mass spectrum of aZnMIm in Figure 3g in the presence of a pronounced peak at m/z = 81. This peak corresponds to the deprotonated 2-methylimidazolate parent ion present throughout the film, as indicated by depth profiling in Figure S17a. A family of peaks at lower m/z indicates the partial fragmentation of the linker under primary ion irradiation, most notably into cyanide at m/z = 26. These cyanide fragments appear to bond strongly with nearby zinc ions in the framework, generating $[Zn(CN)_3]^-$ ions detected in the m/z = 142−146 range, whose relative intensities reflect the isotopic abundance of zinc. Peaks at m/z = 25 and 65 are assigned to C_2H^- and $C_3HN_2^-$, respectively. A peak at m/z = 1, attributed to hydride, is present in high abundance compared to the other peak intensities. A strong peak at m/z = 42 is also present. This peak may correspond to azide, N_3^-, although multiple bonds would need to be broken and formed during ion bombardment of 2-methylimidazolate for its formation. An alternative and more likely assignment of this peak is to one of two possible structures: $C_2H_4N^-$, a structure that can be extracted from the 2-methylimidazolate ion directly by assuming only bond cleavage and proton rearrangement; or cyanate, OCN^-, generated from the combination of surface oxygen with cyanide.

The mass spectrum of aZnMIm exposed to a very high EUV dose of 4036 mJ/cm^2 is given as Figure 3h. Several differences are apparent compared to Figure 3g; notably, the relative hydride signal is significantly depressed. This aligns with the conclusion drawn from the outgassing spectrum that H_2 is generated from the decomposition of 2MIm. Considering a significant portion of hydrogen is lost from the sample, other fragments appearing on the same spectrum are likely lean in hydrogen. The peak at m/z = 42 (present also in the as-deposited films before exposure) can be attributed either to $C_2H_4N^-$ from 2-methylimidazolate or to azide due to the lack of hydrogen in this case. While the relative intensity of the 2-methylimidazolate peak at m/z = 81 is lower when compared to as-deposited aZnMIm, the peak is still present in significant quantity throughout the film (Figure S17b) even after exposure to an extremely high EUV dose. This observation, along with high counts at m/z = 26 (cyanide) and the slight increase in other peaks, such as those at m/z = 50 (cyanoethynyl anion) and m/z = 66 (dicyanamide anion), implies significant but incomplete fragmentation of the 2MIm linkers rather than full transformation to an amorphous matrix composed of carbon, nitrogen, and zinc. This is in contrast to the effects of high doses of electron irradiation where no detectable 2MIm peaks were observed by infrared reflection−absorption spectroscopy (IRRAS).[48] This helps to explain why the development of EUV-exposed aZnMIm using hfacH produces relatively poor sensitivity, as a high EUV dose is required to degrade 2MIm linkers sufficiently to prevent the reaction with hfacH from producing volatile species that lead to etching during vapor development.

Higher mass fragments in the EUV-exposed spectrum in Figure 3h transition from recognizable molecular anions into clusters of peaks with Gaussian-like intensity distributions centered around increasing m/z. These groupings are present in the original aZnMIm mass spectrum as well, but at lower intensity. Their amplification may reflect the formation of high-mass clusters of carbon and nitrogen with the general formula $C_aN_bH_x$ formed from partially fragmented 2MIm with undefined chemical structures. Thus, $C_3HN_2^-$ and $C_2N_3^-$ represent five-atom clusters, while six-atom clusters center near m/z = 80. It can be reasoned that the higher-mass groupings are then composed of larger atom clusters: signals centered around m/z = 119, for example, correspond to nine-atom clusters with an average mass per atom of approximately 13 amu (119/9 = 13.2). Because multiple peaks are visible within these high-mass groupings, their formation is suggestive of multiple individual molecular fragments and extensive atomic rearrangements following EUV exposure.

When compared to the undeveloped spectrum in Figure 3h, EUV-exposed aZnMIm developed in water (Figure 3i) shows slight differences, most notably, the low relative intensity of the m/z = 81 peak, which indicates that 2MIm is nearly, if not entirely, depleted from the sample, consistent with XPS results in Figure S7. A loss of intensity of 2MIm fragments at m/z = 42, 50, and 65 is also observed. It is worth noting that of the slight differences between undeveloped and developed samples, most represent a decrease in the peaks associated with pristine aZnMIm, supporting the conclusion that intact and fragmented 2-methylimidazolate is dissolved during development. Interestingly, the group of peaks corresponding to $[Zn(CN)_3]^-$ are not visible on the developed sample spectrum. Depth profiling of the developed sample (Figure S17c) reveals a depletion of multiple species near the sample surface but slow recovery of Zn species, O^-, and other 2MIm fragments deeper into the film. Moreover, the integrated mass

https://doi.org/10.1021/acs.chemmater.5c01476
Chem. Mater. 2025, 37, 8548−8567

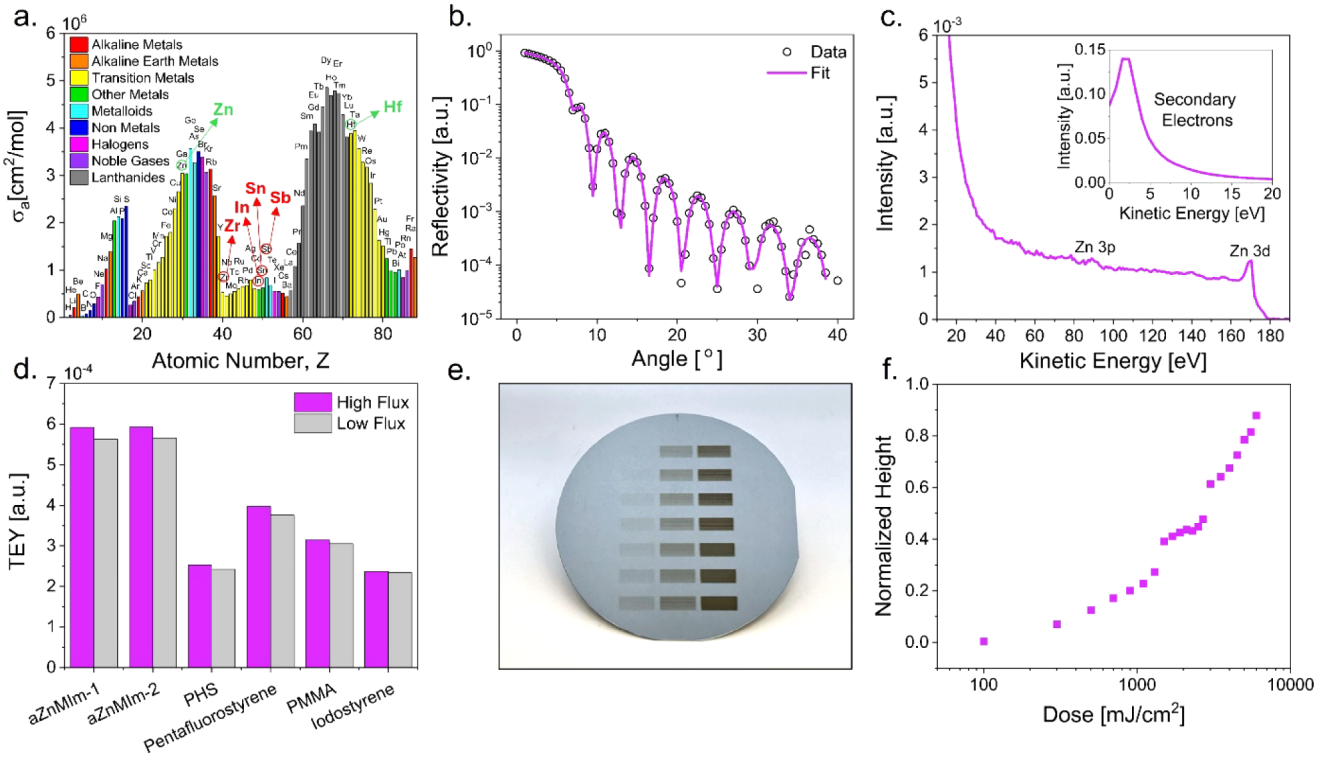

Figure 4. aZnMIm response to a BEUV wavelength of 6.7 nm. (a) Atomic absorption cross-sections at a wavelength of 6.7 nm (185.05 eV). Elements with atomic numbers from 1 to 88 were plotted using atomic scattering factors from the CXRO X-ray database.[106] (b) Reflectometry data obtained experimentally and model fit for a 45 nm thick aZnMIm film to determine BEUV absorption. (c) BEUV photoelectron spectrum of an aZnMIm film showing the distribution of primary and secondary electrons. The inset shows a zoomed-in view of the low-energy secondary electrons (<20 eV). (d) TEY for many model photoresist materials at a wavelength of 6.7 nm. Two aZnMIm locations were tested along with PHS, poly(pentafluorostyrene), PMMA, and poly(iodostyrene). (e) BEUV exposure of a 45 nm thick aZnMIm film at doses between 100 and 6000 mJ/cm^2. Following BEUV, the aZnMIm film was exposed to hfacH vapor at 120 °C for 60 s and then rinsed with methanol. (f) A contrast curve corresponding to the film in (e) with BEUV exposure spots measured via spectroscopic ellipsometry and then normalized with respect to the original film thickness after MLD.

spectrum with respect to depth (Figure S17d) shows a high incidence of zinc and cyanide throughout the developed film but nearly no 2MIm. As such, we conclude that the water-based development dissolves away 2MIm and exposed zinc at the film surface.

Based on the results from multiple EUV characterization methods including EUV PES, reflectometry/EUV absorption, RGA, and TEY, it can be concluded that aZnMIm resist films, which have an EUV absorption coefficient of 6.2 μm^{-1}, have similar EUV absorption properties to Zr-oxo cluster-based resists ($\sigma \sim 6-7\ \mu m^{-1}$),[111] which are slightly more sensitive than polymer-type photoresists. aZnMIm resists show EUV absorption and TEY nearly identical to those of PMMA and are significantly less EUV sensitive than the industry-standard metal-containing SnOx-type resists, which have a high density of EUV-absorptive Sn atoms. These findings support the argument that EUV sensitivity is determined more by the film composition and the inclusion of highly absorptive elements than by specific resist chemistry. While aZnMIm films contain Zn atoms, the metal content is low (C:N:Zn ratio of 9.4:3.4:1),[48] resulting in a resist whose absorption properties are nearly the same as if there were no metal atoms. Compared to PHS and other similar resists, aZnMIm films generate more secondary and primary electrons, as demonstrated by PES and TEY, but have a lower ratio of slow-to-fast electrons, indicating a material with less efficient conversion of primary electrons to secondary electrons. Outgassing of aZnMIm during EUV exposure results in the emission of primarily H_2 but also 2MIm fragments. CO_2 is also detected, but it may be at least in part attributed to sample and/or instrument contamination. TOF-SIMS analysis reveals that high-dose EUV exposure promotes only partial fragmentation of 2MIm organic linkers, unlike high-dose electron beam exposure, which fully degrades 2MIm.[48] Interestingly, during water development, the intact 2MIm molecules in the exposed areas are removed, leaving a nearly 2MIm-free resist in these areas.

BEUVL Response Characteristics of aZnMIm Resists. Wavelengths shorter than 13.5 nm have been proposed as candidates for future lithographic patterning technology nodes, with a wavelength of 6.*x* nm (6.5−6.7 nm) being suggested as a potential candidate for BEUVL.[8,125,126] To realize 6.*x* nm optical lithography, optimization of the light source, reflective optics, photoresist materials, and other HVM challenges must be addressed.[127−130] In terms of photoresist development, early studies predict that optical properties and photoresist sensitivities will change significantly from 13.5 nm to 6.*x* nm due to sharp differences in optical absorption properties.[8,130,131]

Using data available in the CXRO X-ray database,[106] BEUV atomic absorption cross-sections at a wavelength of 6.7 nm were calculated and plotted as a function of atomic number in Figure 4a. The equations used for calculating BEUV atomic absorption cross-sections are included in Section S3. When compared to the elemental absorption cross-sections at 13.5

https://doi.org/10.1021/acs.chemmater.5c01476
Chem. Mater. 2025, 37, 8548−8567

nm,[110] it is clear that absorption is lower for elements at 6.7 nm; however, the overall trend in absorption changes significantly, with common EUV photoresist metals like Sn, In, Sb, and Zr becoming very low absorbers at BEUV wavelengths, while transition metals like Zn and Hf are some of the highest absorbers. As such, Zn-containing aZnMIm resists could be potential candidates for next-generation BEUVL photoresists.

Because the ALS at Berkeley National Laboratory can be easily tuned to wavelengths in the BEUVL range (6.5−6.7 nm), BEUV reflectometry, PES, and TEY measurements were repeated to determine the BEUV response characteristics of aZnMIm resists. Similar to how 13.5 nm was selected as the wavelength of choice for EUVL, the wavelengths used for BEUVL were selected guided by the reflectivity performance of top-performing multilayer mirrors. Among the most efficient are La/B, La/B_4C, and Mo/B_4C multilayer systems, which demonstrate peak reflectivities of 60−80% near 6.7 nm.[132−134] Depending on the literature reference, the optimal performance of these mirrors is reported at a wavelength of either 6.65 nm[132,133] or 6.7 nm.[134] Based on this information, we performed reflectometry measurements in the 6.6−6.7 nm range to evaluate light absorption. These data are presented in Figures S18 and 4b for measurements at 6.6/6.65 and 6.7 nm, respectively. The resulting linear attenuation coefficients were found to increase monotonically with wavelength—from 2.68 μm^{-1} at 6.6 nm to 2.72 μm^{-1} at 6.7 nm. These values are relatively low compared to those reported for EUV wavelengths because the attenuation coefficients are expected to decrease as incident photon absorption is generally lower at higher photon energies.[130,131] For a 20 nm aZnMIm resist, the corresponding BEUV absorption ranges from 5.22% to 5.29%, depending on the exact wavelength. Because 6.7 nm showed the most promising behavior and is the most likely candidate for BEUVL, all subsequent characterizations were conducted at a wavelength of 6.7 nm, corresponding to a photon energy of 185.05 eV.

The photoelectron spectrum collected during irradiation at 6.7 nm is shown in Figure 4c. The spectrum exhibits an onset of electron emission at a kinetic energy of approximately 180 eV. Near the onset, a pronounced feature appears in the valence band, corresponding to the photoemission of Zn 3*d* electrons. The rest of the spectrum is largely featureless, aside from a small peak at around 90 eV, likely due to Zn 3*p* emission. According to Yeh et al., the photoionization cross-section for the Zn 3*p* level at this energy is significantly lower than that for the Zn 3*d* level, resulting in a barely visible peak in the photoelectron spectrum.[135] Below a kinetic energy of 20 eV, the spectrum is dominated by slow secondary electron emission. Comparing the photoelectron spectrum of aZnMIm with that of the common photoresist PHS in Figure S19 reveals that during exposure to a wavelength of 6.7 nm, aZnMIm emits more photoelectrons than PHS. The PHS spectrum is nearly featureless except for a peak around 78 eV, corresponding to Si 2*p* electron emission from the substrate. Due to the low thickness (∼10 nm) of the PHS film, some of these substrate-emitted electrons can traverse the film and be detected. A comparison of the ratio of slow to fast electrons, which reflects the yield of secondary electrons per primary electron, yields a ratio of 3.59 for aZnMIm which is slightly lower than the 4.05 observed for PHS. This trend mirrors the previous observations at EUV wavelengths, although the absolute values are reduced.

Figure 4d presents the TEY from several materials, including two different locations from an aZnMIm film. The measurements show that aZnMIm emits nearly twice as many electrons as PHS at 6.7 nm. Furthermore, the TEY from aZnMIm surpasses that of PMMA, poly(pentafluorostyrene), and poly(4-iodostyrene), with the latter two being known for their high EUV TEYs. Despite these advantages, the absolute electron yield at 6.7 nm remains approximately half of that observed under EUV exposure, consistent with the lower light absorption in this wavelength range.

Based on these promising observations, BEUV exposure at a wavelength of 6.7 nm was conducted at the ALS at Berkeley National Laboratory, exposing a 45 nm thick aZnMIm film to 21 different doses ranging from 100 to 6000 mJ/cm^2, as depicted in Figure 4e. The dose corresponding to each exposure is shown in Figure S20. Following exposure, the film was developed using hfacH vapor at 120 °C for 60 s followed by a methanol rinse. All exposure spots apart from 100 mJ/cm^2 are clearly visible by eye after development. After exposure spot heights were extracted using ellipsometry, the heights were normalized with respect to the original height of the film measured after MLD and then plotted against dose to give the BEUV contrast curve for aZnMIm shown in Figure 4f. Consistent with the behavior observed at EUV exposure wavelengths for dry-developed aZnMIm, the measured height continues to increase with dose rather than leveling off at high doses to give the classic sigmoidal contrast curve shape. Calculation of the lithographic parameters reveals a BEUV sensitivity of 2741 mJ/cm^2 and a lithographic contrast of 0.56. While the contrast did not significantly change as a result of decreasing wavelength, a 7x increase in required dose was observed, similar to experimental observations by Anderson and coworkers where the sensitivity of an organic CAR resist at 6.7 nm was shown to be a factor of 6 lower than the sensitivity at 13.5 nm.[130]

CONCLUSION

In summary, it was demonstrated for the first time that amorphous zinc-imidazolate (aZnMIm) resists, which have previously shown capability as high-resolution electron beam resists, can also function as negative-tone EUV photoresists. While water development of EUV-exposed aZnMIm produces a high sensitivity of 5 mJ/cm^2, significant residue in the nonexposed areas prevents water from being used as an effective developer. Acetic acid development, on the other hand, results in rapid dissolution of both exposed and nonexposed regions, leading to poor contrast. A hybrid development method—initial water development followed by acetic acid—achieved more selective removal of nonexposed material while retaining EUV-treated areas, resulting in residue-free development and a sensitivity of 181 mJ/cm^2. Dry development of EUV-exposed aZnMIm using 1,1,1,5,5,5-hexafluoroacetylacetone (hfacH) was also demonstrated; however, low sensitivity and contrast were observed. Several experimental techniques, including EUV PES, reflectometry, TEY, RGA, and TOF-SIMS, were employed to study EUV-exposed aZnMIm thin films. Reflectometry revealed that aZnMIm resists have EUV absorption properties similar to those of Zr-oxo cluster-based resists, which are slightly more sensitive than polymer-type photoresists. EUV PES analysis shows that, compared to PHS, aZnMIm emits more primary and secondary electrons, while TEY experiments reveal an electron yield similar to that of PMMA. RGA shows that when

https://doi.org/10.1021/acs.chemmater.5c01476
Chem. Mater. 2025, 37, 8548−8567

exposed to EUV, aZnMIm predominantly outgasses H_2 while TOF-SIMS measurements demonstrate that high-dose EUV exposure partially fragments the 2MIm organic linkers. For the first time, aZnMIm resists were investigated for their performance as potential next-generation BEUV photoresists due to their inclusion of Zn metal atoms, which show high sensitivity at a wavelength of 6.7 nm. TEY measurements demonstrate that aZnMIm emits nearly twice as many electrons as PHS at 6.7 nm. Furthermore, the TEY from aZnMIm surpasses those of PMMA, poly(pentafluorostyrene), and poly(4-iodostyrene). This work provides a deeper understanding of how ZIF-based materials interact with EUV light and shows for the first time the potential of amorphous ZIF materials to function as both wet and dry developable EUV photoresists as well as BEUV resists. Future work will focus on tuning material chemistry to increase lithographic properties, as well as investigating high-resolution patterning.

EXPERIMENTAL SECTION

Materials. Diethylzinc (DEZ) (95%, Strem Chemicals), 2-methylimidazole (2MIm) (99%, Millipore-Sigma), methanol (99.8%, Fisher Scientific), acetic acid (99.7%, Sigma-Aldrich), tetramethylammonium hydroxide (TMAH) (25 wt % in H_2O, Sigma-Aldrich), poly(4-hydroxystyrene) (Polymer Source, Inc.), poly(methyl methacrylate) (Polymer Source, Inc.), poly(pentafluorostyrene) (Polymer Source, Inc.), poly(4-iodostyrene) (Polymer Source, Inc.), propylene glycol methyl ether (PGME) (Sigma-Aldrich), propylene glycol methyl ether acetate (PGMEA) (Sigma-Aldrich), nitrogen (N_2) gas (>99.999%, AirGas), and argon (Ar) gas (>99.999%, AirGas) were used as received without further purification. 1,1,1,5,5,5-hexafluoroacetylacetone (hfacH) (98%, Sigma-Aldrich) was purified with three freeze-pump-thaw cycles before use. Homemade Milli-Q DI water (H_2O) was used. Silicon (100) wafers were purchased from UniversityWafer Inc. A custom-designed mask with a SiC membrane and electroplated gold gratings was fabricated at Applied Nanotools Inc. 1 Mil Kapton tape was purchased from Uline.

Ellipsometry. Film thicknesses were measured by using a Film Sense FS1 ellipsometer using four LEDs with wavelengths between 465.27 and 641.13 nm. SiO_2 thickness was measured using the built-in SiO_2 on Si model, and the deposited film thickness was measured with a Cauchy model.

Spectroscopic Ellipsometry. All samples apart from the samples shown in Figures 2c, S11, and 4e were measured using a J. Woollam M-2000X Spectroscopic Ellipsometer over the spectral range of 1.3−6.45 eV; film thickness was extracted using a model comprised of a Cauchy thin film on a Si substrate. The film depicted in Figures 2c and S11 was measured by using a Bruker FilmTek 2000 PAR-SE Spectroscopic Ellipsometer with a spot size of 50 μm. The sample shown in Figure 4e was measured using a J. Woollam M-2000X Spectroscopic Ellipsometer over the spectral range of 1.1−3.1 eV.

Scanning Electron Microscopy (SEM). SEM images were acquired with a ThermoFisher Helios G4 UC DualBeam at an acceleration voltage of 5 kV and a current of 100 pA.

Optical Microscopy. An Olympus BX53MTRF-S instrument was used for optical micrograph imaging. The sample of interest was placed onto the stage and focused using a 5x objective. The micrograph was obtained using the panorama function and focused using an image map. If required, images were processed with GIMP to combine the individual scans into a single focused image.

X-ray Photoelectron Spectroscopy (XPS). XPS spectra were acquired on a nonmonochromatic PHI 5600 XPS using 1253.6 eV Mg Kα X-rays at a power of 300 W. Survey scans were acquired at a pass energy of 178.95 eV. High-resolution scans were acquired at a pass energy of 23.5 eV.

EUV Exposure. EUV exposure was conducted at EUV Tech Inc. on an experimental general-purpose EUV flood exposure tool in a cleanroom. A 100 mm Si wafer was coated with between 15 and 100 nm of aZnMIm at JHU before being packaged and vacuum-sealed in air. At EUV Tech Inc., the wafers were loaded vertically into a high-vacuum chamber and pumped down. The EUV source was started, and a diode was inserted between the sample and beam to measure the beam current. After recording the current, the diode was removed, and a recipe was loaded. The wafer was rotated to 0° before the shutter was opened for a set amount of time. The shutter automatically closed and rotated 45° before the shutter was opened again for the desired time. This process was repeated six more times to expose a total of eight locations, each 45° apart. After all eight locations were exposed, the diode was inserted and the beam current was recorded again. The beam was shut off, and the system was vented. After being vented, the sample was removed from the chamber. To calculate the exposure dose, the flood spot area (which looked to be approximately 2.5 × 5 mm) was measured on a nondeveloped sample latent image using ImageJ and was found to be 0.103 cm^2 (Figure S21). The pre- and postexposure current measured from the diode was averaged. The EUV dose was determined using the equation below, where time (s) is the duration for the shutter remaining open in a recipe:

$$\text{Dose}\left(\frac{\text{mJ}}{\text{cm}^2}\right) = \text{current (mA)} \times \frac{1\ \text{mW}}{0.09\ \text{mA}} \times \frac{1\ \text{mJ/s}}{1\ \text{mW}} \times \frac{\text{time (s)}}{\text{spot area (cm}^2\text{)}} \quad (3)$$

Line Patterning with EUV Flood Exposure Tool. Line patterning was conducted using the EUV exposure tool at EUV Tech Inc. A 100 mm Si wafer was coated with between 15 and 100 nm of aZnMIm at JHU before being packaged and vacuum-sealed in air. Once at EUV Tech Inc., the spot location on a developed sample was measured and found to be approximately 16.5 mm from the center of the wafer. A custom-made coarse grating mask from Applied Nanotools Inc. was used for line patterning. The mask was 5 mm × 5 mm with a 1.1 mm × 1.1 mm window. The mask was placed onto the resist-coated wafer with the central window 16.5 mm away from the center (35.5 mm away from the rounded wafer edge). The mask was then taped onto the wafer with Kapton tape. The wafer with the attached mask was loaded vertically into a high-vacuum chamber and pumped down. While pumping down, start and stop points for EUV exposure were determined. Based on the location of the 1.1 mm × 1.1 mm window 16.5 mm away from the center of the wafer, the required beam speed was calculated so that the beam exposed the 1.21 mm^2 area for the desired amount of time. The desired amount of time was scaled based on the transmittance of the SiC mask membrane, which is reported to be 64% at 13.5 nm (Figure S3). The EUV source was started, and a diode was inserted between the sample and the beam to measure the beam current. After the current was recorded, the diode was

https://doi.org/10.1021/acs.chemmater.5c01476
Chem. Mater. 2025, 37, 8548−8567

removed. The beam was swept from the start point to the stop point at the entered beam speed with the beam shutter open. Once finished, the shutter was closed, the diode was inserted, and the beam current was recorded again. The beam was shut off, and the system was vented. After venting, the sample was removed from the chamber.

Liquid Development. A 655 μM acetic acid solution was prepared by diluting glacial acetic acid with DI water. 0.265 and 0.55 M TMAH solutions were prepared by diluting 25 wt % TMAH with DI water. For batch development, a 5 in. × 5 in. dish was filled with 150 mL of DI water, 655 μM acetic acid, methanol, or 0.265/0.55 M TMAH solution. The wafer was inserted into the developer and gently agitated for the desired time. The wafer was then removed from the developer. Films developed in water were immediately dried with pressurized nitrogen or compressed air. Films developed in acetic acid were removed from the developer and rinsed with methanol before being dried with pressurized nitrogen or compressed air. For flow development, a homemade flow device was 3D-printed and set up as described elsewhere.[66] In brief, a silicon wafer was placed into the device, and a PDMS-coated glass slide (7.5 cm × 1.5 cm) was placed on top of the device. A 60 mL syringe was filled with DI water and mounted on a syringe pump. During dissolution, water was injected into the device through silicone tubing at a flow rate of 2 mL/min. For spin-off development, a wafer was placed into a spin coater, and a 60 mL syringe was filled with DI water before being mounted into a syringe pump. The wafer was spun at 2000 rpm, while water was introduced above the spinning wafer at a flow rate of 2 mL/min.

Dry Deposition of Amorphous Zinc-Imidazolate Thin Films by Atomic/Molecular Layer Deposition (ALD/MLD). The deposition of aZnMIm films was carried out according to previous experiments.[48] In brief, 100 mm silicon (100) wafers to be used as substrates were cleaned by sonication in ethanol. The native SiO_2 film thickness was measured by ellipsometry, and substrates with an oxide film thickness of >2.2 nm were not used. DEZ and 2MIm were pulsed sequentially into a home-built flow-through MLD reactor with intermittent Ar gas purges. The DEZ precursor cylinder was maintained at ambient temperature, and the 2MIm precursor cylinder was placed in a box oven heated to 150 °C with the reactor. Pulse lengths of DEZ and 2MIm were fixed at 50 and 100 ms, respectively. Purge lengths of 30 s for DEZ and 45 s for 2MIm were used. The precursor inlet and reactor outlet lines were heated to 100 °C to prevent condensation of 2MIm and DEZ. The Ar flow rate in the reactor was set to 10 sccm.

Dry Development. Films were placed in a quartz tube reactor with stainless-steel fittings and heated to 120 °C in an oven. The system was evacuated to a base pressure of 0.05 mbar before imposing a 5 sccm argon flow at a pressure of 2 mbar. The system was left to be evacuated for 30 min. After 30 min, the argon flow was turned off and the system was allowed to purge for another 60 s. Subsequently, the valve to the pump was turned off, and the hfacH valve was opened for 2 s. The sample was exposed to a static hfacH pressure of 6.5 mbar for the desired time of 10−60 s. Finally, the system was evacuated under dynamic vacuum with a 5 sccm argon flow for 30 min and then allowed to cool to room temperature.

Direct-Write Electron Beam Lithography. EBL patterning experiments were conducted on a ThermoFisher Helios G4 UC Focused Ion Dual Beam Microscope. An acceleration voltage of 5 kV was chosen, and a beam current of 100 pA was used. All patterns were exposed for a dwell time of 1 μs, while the pass (scan) number was varied in each exposure to obtain the desired electron dose. The electron dose was calculated as a function of the pixel size, current, number of scans, and dwell time. Pattern files were generated in Adobe Photoshop with a pixel density of 454 pixels per inch and a pixel size of 2.1 nm.

Reflectometry/EUV Absorption Analysis. EUV absorption measurements were performed at the ALS beamline 6.3.2 at the Lawrence Berkeley National Laboratory using the reflectivity method.[112] Reflectivity measurements at 13.5 nm were conducted by using a 200 mm^{-1} grating, a Be filter, and a photodiode detector. The components of the complex refractive index $\tilde{n}$ are given as:

$$\tilde{n} = 1 - \delta + i\beta \tag{4}$$

where δ is the dispersive component and β is the absorptive component of the refractive index of the polymer film. The imaginary part of the refractive index is obtained by fitting the experimental data. From the obtained value of β, the linear attenuation coefficient, μ ,of the polymer is calculated using the following equation:

$$\mu = \frac{4\pi}{\lambda} \times \beta \tag{5}$$

where λ is the irradiation wavelength.

Photoelectron Spectroscopy. A custom-built PES instrument, installed at ALS beamline 12.0.1.2, was used to analyze EUV-sensitive materials. During the measurement, the sample is exposed to EUV radiation and the emitted electrons are collected using a retarding field analyzer. The instrument features the continuous movement of the sample in front of the detector, ensuring that the photoelectron signal is collected from a fresh, unexposed region of the film. This minimizes the impact of EUV exposure during the measurement, which is critical for EUV-sensitive materials. The estimated EUV dose during the measurement is approximately 2 mJ/cm^2, which is generally below the sensitivity of known EUV resists.

Deposition of Polymer Films for PES and TEY Analysis. Thin films of polymers, such as poly(4-hydroxystyrene), poly(4-iodostyrene), poly(pentafluorostyrene), and poly(methyl methacrylate), were prepared from ∼5 mg/mL solutions of polymer powder in a 1:1 mixture of PGME and PGMEA. The solutions were spin-coated onto 100 mm Si wafers to achieve a uniform film thickness of approximately 10−17 nm. Following spin-coating, the samples underwent a postapplication bake at 110 °C for 60 s.

Total Electron Yield. The TEY technique measures the current generated by electrons emitted from a sample during EUV exposure. The measurement was performed at the ALS beamline 6.3.2. The measured drain current is normalized by the photon flux, which is measured with a silicon photodiode. The resulting TEY is determined as the electron yield per unit of photon flux.

Residual Gas Analysis for Resist Outgassing. Outgassing measurements were conducted at ALS beamline 12.0.1.2. The experimental setup[136] utilized a sample holder capable of accommodating up to 50 samples on 10 × 10 mm^2 Si wafer coupons, significantly increasing the measurement throughput. Moderate EUV photon flux levels (1.3 $mJ/cm^2/s$) were employed to balance signal clarity with detector sensitivity, enabling the capture of time-dependent changes in the

https://doi.org/10.1021/acs.chemmater.5c01476
Chem. Mater. 2025, 37, 8548−8567

outgassing signals. The outgassing measurement was performed using a residual gas analyzer manufactured by Stanford Research Systems Inc., capable of detecting mass-to-charge ratios ranging from 1 to 300. Background signals, recorded in the absence of EUV exposure, were subtracted from the outgassing signals to isolate species released from the resist during irradiation. The resulting outgassing spectra allowed for the identification of specific chemical species and tracked their evolution over exposure time.

Time-of-Flight Secondary Ion Mass Spectrometry. TOF-SIMS experiments were performed similarly to those described elsewhere.[137] In brief, an ION TOF M6 spectrometer with a Bi_3 primary ion source was used with the analyzer set to detect negative ions. During the analysis, the flood gun was active to prevent surface charging. An individual scan measured the mass spectrum of a 100 μm^2 region of the sample surface, recording 20 frames in total. Depth profiling was done by sputtering a 300 μm^2 region with 1200-atom argon clusters at 5 keV/4 nA and recording 4 frames of a 100 μm^2 region within the raster every 3 s, for 80 s of sputtering in total.

■ ASSOCIATED CONTENT

Data Availability Statement

The data that support the findings of this study are available from the corresponding author upon reasonable request.

Supporting Information

The Supporting Information is available free of charge at https://pubs.acs.org/doi/10.1021/acs.chemmater.5c01476.

2MIm and Zn speciation calculations, aZnMIm density calculations, calculation of BEUVL atomic absorption cross-sections, experimental setup, material EUV transmission, pattern fabrication, dissolution and characterization of aZnMIm in water and other solvents, XPS, ellipsometry, EUV and BEUV PES of PHS thin films, Si wafer outgassing, isolated ion signals for significant m/z, TOF-SIMS depth profiling, reflectometry at 6.6 and 6.65 nm, EUV and BEUV doses and dose calculation (PDF)

■ AUTHOR INFORMATION

Corresponding Authors

Oleg Kostko − *Center for X-Ray Optics, Materials Sciences Division, Lawrence Berkeley National Laboratory, Berkeley, California 94720, United States;* orcid.org/0000-0003-2068-4991; Email: okostko@lbl.gov

Michael Tsapatsis − *Department of Chemical and Biomolecular Engineering and Institute for Nanobiotechnology, Johns Hopkins University, Baltimore, Maryland 21218, United States; Applied Physics Laboratory, Johns Hopkins University, Laurel, Maryland 20723, United States;* orcid.org/0000-0001-5610-3525; Email: tsapatsis@jhu.edu

Authors

Kayley E. Waltz − *Department of Chemical and Biomolecular Engineering and Institute for Nanobiotechnology, Johns Hopkins University, Baltimore, Maryland 21218, United States*

Xinpei Zhou − *Department of Chemical and Biomolecular Engineering and Institute for Nanobiotechnology, Johns Hopkins University, Baltimore, Maryland 21218, United States*

Xavier Krull − *Department of Chemistry, Northwestern University, Evanston, Illinois 60208, United States;* orcid.org/0000-0002-3608-8441

Somya Singh − *Department of Chemical and Biomolecular Engineering and Institute for Nanobiotechnology, Johns Hopkins University, Baltimore, Maryland 21218, United States*

Eric Mattson − *Intel Corporation, Foundry Technology Research, Hillsboro, Oregon 97124, United States*

Yurun Miao − *Department of Chemical and Biomolecular Engineering and Institute for Nanobiotechnology, Johns Hopkins University, Baltimore, Maryland 21218, United States;* orcid.org/0000-0001-6429-8297

Matt Hettermann − *EUV Tech Inc., Martinez, California 94553, United States*

Travis Grodt − *EUV Tech Inc., Martinez, California 94553, United States*

Qi Zhang − *Center for X-Ray Optics, Materials Sciences Division, Lawrence Berkeley National Laboratory, Berkeley, California 94720, United States;* orcid.org/0000-0002-2915-7605

Honggu Im − *Center for X-Ray Optics, Materials Sciences Division, Lawrence Berkeley National Laboratory, Berkeley, California 94720, United States*

Bernhard Lüttgenau − *Center for X-Ray Optics, Materials Sciences Division, Lawrence Berkeley National Laboratory, Berkeley, California 94720, United States*

Lauren Doyle − *Intel Corporation, Foundry Technology Research, Hillsboro, Oregon 97124, United States*

Andrea Kraetz − *Department of Chemical and Biomolecular Engineering and Institute for Nanobiotechnology, Johns Hopkins University, Baltimore, Maryland 21218, United States*

Max Beutner − *Department of Chemical and Biomolecular Engineering and Institute for Nanobiotechnology, Johns Hopkins University, Baltimore, Maryland 21218, United States;* orcid.org/0009-0005-1979-3826

Scott B. Clendenning − *Intel Corporation, Foundry Technology Research, Hillsboro, Oregon 97124, United States*

D. Howard Fairbrother − *Department of Chemistry, Johns Hopkins University, Baltimore, Maryland 21218, United States;* orcid.org/0000-0003-4405-9728

Joseph T. Hupp − *Department of Chemistry, Northwestern University, Evanston, Illinois 60208, United States;* orcid.org/0000-0003-3982-9812

Patrick Naulleau − *EUV Tech Inc., Martinez, California 94553, United States; Center for X-Ray Optics, Materials Sciences Division, Lawrence Berkeley National Laboratory, Berkeley, California 94720, United States*

Lawrence Rooney − *Bruker Nano Inc., San Jose, California 95134, United States*

Complete contact information is available at: https://pubs.acs.org/10.1021/acs.chemmater.5c01476

Notes

The authors declare the following competing financial interest(s): J. T. H. has an equity interest in NuMat, a company that commercializes MOFs.

■ ACKNOWLEDGMENTS

This work was supported by the Bloomberg Distinguished Professorship program, the Whiting School of Engineering at

Johns Hopkins University, and the National Science Foundation (NSF ECCS-2428276). ALD/MLD experiments were supported by the U.S. Department of Energy, Office of Science, Office of Basic Energy Sciences, Division of Chemical Sciences, Geosciences, and Biosciences under award DE-SC0021212. J.T.H. acknowledges support by the Catalyst Design for Decarbonization Center, an Energy Frontier Research Center (EFRC) funded by the U.S. Department of Energy, Office of Science, Basic Energy Sciences (DE-SC0023383). This research used resources of the Advanced Light Source, a U.S. DOE Office of Science User Facility (Grant No. DE-AC02-05CH11231). EBL was performed at the Materials Characterization and Processing Center in the Whiting School of Engineering at Johns Hopkins University. TOF-SIMS was performed in the Keck-II facility (RRID: SCR_026360) of Northwestern University's NUANCE Center, which has received support from the SHyNE Resource (NSF ECCS-2025633), the IIN, and Northwestern's MRSEC program (NSF DMR-2308691). The authors are grateful to Rob Peters and the staff at Applied Nanotools Inc. for assistance in designing and fabricating the mask used for EUV patterning. The authors would also like to acknowledge Caroline Anastasia for her assistance with XPS analysis and Isabelle Simpliphant for her help with dissolution experiments.

REFERENCES

(1) Silverman, P. J. Extreme Ultraviolet Lithography: Overview and Development Status. *J. Micro/Nanolithogr., MEMS, MOEMS* **2005**, *4*, 011006.

(2) Wu, B.; Kumar, A. Extreme Ultraviolet Lithography: A Review. *J. Vac. Sci. Technol. B* **2007**, *25*, 1743−1761.

(3) Buitrago, E.; Kulmala, T. S.; Fallica, R.; Ekinci, Y. EUV Lithography Process Challenges. *Front. Nanosci.* **2016**, *11*, 135−176.

(4) Fallica, R.; Rezvani, S. J.; Nannarone, S.; Borisov, S.; De Simone, D.; Babin, S.; Lorusso, G.; Vandenberghe, G. The Hidden Energy Tail of Low Energy Electrons in EUV Lithography. *Advances in Patterning Materials and Processes XXXVI* **2019**, *10960*, 1096009.

(5) Torok, J.; Del Re, R.; Herbol, H.; Das, S.; Bocharova, I.; Paolucci, A.; Ocola, L. E.; Ventrice, C., Jr; Lifshin, E.; Denbeaux, G.; et al. Secondary Electrons in EUV Lithography. *J. Photopolym. Sci. Technol.* **2013**, *26* (5), 625−634.

(6) Bespalov, I.; Zhang, Y.; Haitjema, J.; Tromp, R. M.; van der Molen, S. J.; Brouwer, A. M.; Jobst, J.; Castellanos, S. Key Role of Very Low Energy Electrons in Tin-Based Molecular Resists for Extreme Ultraviolet Nanolithography. *ACS Appl. Mater. Interfaces* **2020**, *12*, 9881−9889.

(7) van Schoot, J.; van Ballegoij, R.; Butler, H.; van Setten, E.; Schiffelers, G.; Bouman, W.; van Gorp, S.; Umstadter, K.; Zimmermann, J.; Golde, D.; et al. Next Step in Moore's Law: High NA EUV System Overview and First Imaging and Overlay Performance. *J. Micro/Nanopattern. Mater. Metrol.* **2024**, *24*, 011009.

(8) Mojarad, N.; Gobrecht, J.; Ekinci, Y. Beyond EUV Lithography: A Comparative Study of Efficient Photoresists' Performance. *Sci. Rep.* **2015**, *5*, 9235.

(9) Li, L.; Liu, X.; Pal, S.; Wang, S. L.; Ober, C. K.; Giannelis, E. P. Extreme Ultraviolet Resist Materials for Sub-7 nm Patterning. *Chem. Soc. Rev.* **2017**, *46*, 4855−4866.

(10) Saifullah, M. S. M.; Tiwale, N.; Ganesan, R. Review of Metal-Containing Resists in Electron Beam Lithography: Perspectives for Extreme Ultraviolet Patterning. *J. Micro/Nanopattern. Mater. Metrol.* **2022**, *21*, 041402.

(11) Manouras, T.; Argitis, P. High Sensitivity Resists for EUV Lithography: A Review of Material Design Strategies and Performance Results. *Nanomaterials* **2020**, *10*, 1593.

(12) Narasimhan, A.; Grzeskowiak, S.; Srivats, B.; Herbol, H.; Wisehart, L.; Kelly, C.; Earley, W.; Ocola, L. E.; Neisser, M.; Denbeaux, G.et al. Studying Secondary Electron Behavior in EUV Resists Using Experimentation and Modeling. *Extreme Ultraviolet (EUV) Lithography VI* **2015**, *9422*, 942208.

(13) Grenville, A.; Anderson, J. T.; Clark, B. L.; De Schepper, P.; Edson, J.; Greer, M.; Jiang, K.; Kocsis, M.; Meyers, S. T.; Stowers, J. K.et al. Integrated Fab Process for Metal Oxide EUV Photoresist. *Advances in Patterning Materials and Processes XXXII* **2015**, *9425*, 94250S.

(14) Kawakami, S.; Onitsuka, T.; Kamei, Y.; Shimura, S.; Park, C. H.; Lee, S. H.; Lee, H. G.; Seo, J. W.; Il Kim, J.; Ho Roh, J.et al. Metal Oxide Resist (MOR) EUV Lithography Processes for DRAM Application. *Advances in Patterning Materials and Processes XXXIX* **2022**, *12055*, 120550N.

(15) Sharma, S. K.; Chauhan, M.; Kumar, R.; Palit, K.; Choudhary, S.; Gonsalves, K. E. Development of Metal-Organic Cluster Based Negative Tone Resist: Pre-screened Through the Helium-ion Beam Prelude to Extreme Ultraviolet Lithography (EUVL) Applications. *Advances in Patterning Materials and Processes XXXVIII* **2021**, *11612*, 1161208.

(16) Passarelli, J.; Murphy, M.; Del Re, R.; Sortland, M.; Dousharm, L.; Vockenhuber, M.; Ekinci, Y.; Neisser, M.; Freedman, D. A.; Brainard, R. L. High-Sensitivity Molecular Organometallic Resist for EUV (MORE). *Advances in Patterning Materials and Processes XXXII* **2015**, *9425*, 94250T.

(17) Toriumi, M.; Sato, Y.; Kumai, R.; Yamashita, Y.; Tsukiyama, K.; Itani, T. Characterization of 'Metal Resist' for EUV Lithography. *Advances in Patterning Materials and Processes XXXIII* **2016**, *9779*, 97790G.

(18) Shi, J. W.; Ravi, A.; Richey, N. E.; Gong, H. X.; Bent, S. F. Molecular Layer Deposition of a Hafnium-Based Hybrid Thin Film as an Electron Beam Resist. *ACS Appl. Mater. Interfaces* **2022**, *14*, 27140−27148.

(19) Xu, H.; Sakai, K.; Kasahara, K.; Kosma, V.; Yang, K.; Herbol, H. C.; Odent, J.; Clancy, P.; Giannelis, E. P.; Ober, C. K. Metal-Organic Framework-Inspired Metal-Containing Clusters for High-Resolution Patterning. *Chem. Mater.* **2018**, *30*, 4124−4133.

(20) Cardineau, B.; Del Re, R.; Marnell, M.; Al-Mashat, H.; Vockenhuber, M.; Ekinci, Y.; Sarma, C.; Freedman, D. A.; Brainard, R. L. Photolithographic Properties of Tin-Oxo Clusters Using Extreme Ultraviolet Light (13.5 nm). *Microelectron. Eng.* **2014**, *127*, 44−50.

(21) Volosskiy, B.; Weidman, T. W.; Tan, S. S.; Wu, C.; Gu, K. Dry Development of Resists. World Patent WO2020132281A1, **2020**.

(22) Wise, R. S. Breaking Stochastic Tradeoffs with a Dry Deposited and Dry Developed EUV Photoresist System. *Advances in Patterning Materials and Processes XXXVIII* **2021**, *11612*, 1161203.

(23) Weidman, T. M.; Nardi, K. L.; Dictus, D.; Kam, B.; Wu, C.; Hansen, E. C.; Kenane, N.; Gu, K. L. Positive Tone Development of CVD EUV Resist Films. World Patent WO2021072042A1, **2021**.

(24) Dictus, D.; Wu, C.; Hansen, E. C.; Weidman, T. W. Photoresist Development with Organic Vapor. World Patent WO2022125388A1, **2022**.

(25) Valdez, M.; Joshi-Imre, A.; Dunn, B.; Herrera Lara, M.; Hsu, J. W. P. Sensitivity and Contrast of Indium Nitrate Hydrate Resist Evaluated by Low-Energy Electron Beam and Extreme Ultraviolet Exposure. *J. Micro/Nanopattern. Mater. Metrol.* **2025**, *24*, 014601.

(26) Mattson, E. C.; Cabrera, Y.; Rupich, S. M.; Wang, Y. X.; Oyekan, K. A.; Mustard, T. J.; Halls, M. D.; Bechtel, H. A.; Martin, M. C.; Chabal, Y. J. Chemical Modification Mechanisms in Hybrid Hafnium Oxo-methacrylate Nanocluster Photoresists for Extreme Ultraviolet Patterning. *Chem. Mater.* **2018**, *30*, 6192−6206.

(27) Passarelli, J.; Murphy, M.; Del Re, R.; Sortland, M.; Hotalen, J.; Dousharm, L.; Fallica, R.; Ekinci, Y.; Neisser, M.; Freedman, D. A.; et al. Organometallic Carboxylate Resists for Extreme Ultraviolet with High Sensitivity. *J. Micro/Nanolithogr., MEMS, MOEMS* **2015**, *14* (4), 043503.

(28) Zhang, Y.; Haitjema, J.; Baljozovic, M.; Vockenhuber, M.; Kazazis, D.; Jung, T. A.; Ekinci, Y.; Brouwer, A. M. Dual-tone Application of a Tin-Oxo Cage Photoresist Under E-beam and EUV Exposure. *J. Photopolym. Sci. Technol.* **2018**, *31*, 249−255.

https://doi.org/10.1021/acs.chemmater.5c01476
Chem. Mater. 2025, 37, 8548−8567

(29) Del Re, R.; Sortland, M.; Passarelli, J.; Cardineau, B.; Ekinci, Y.; Vockenhuber, M.; Neisser, M.; Freedman, D. A.; Brainard, R. L. Low-LER Tin Carboxylate Photoresists using EUV. *Extreme Ultraviolet (EUV) Lithography VI* **2015**, *9422*, 942221.
(30) Haitjema, J.; Zhang, Y.; Vockenhuber, M.; Kazazis, D.; Ekinci, Y.; Brouwer, A. M. Extreme Ultraviolet Patterning of Tin-Oxo Cages. *J. Micro/Nanolithogr., MEMS, MOEMS* **2017**, *16* (3), 033510.
(31) Wu, L. J.; Baljozovic, M.; Portale, G.; Kazazis, D.; Vockenhuber, M.; Jung, T.; Ekinci, Y.; Castellanos, S. Mechanistic Insights in Zr- and Hf-Based Molecular Hybrid EUV Photoresists. *J. Micro/Nanolithogr., MEMS, MOEMS* **2019**, *18* (1), 013504.
(32) Li, L.; Chakrabarty, S.; Spyrou, K.; Ober, C. K.; Giannelis, E. P. Studying the Mechanism of Hybrid Nanoparticle Photoresists: Effect of Particle Size on Photopatterning. *Chem. Mater.* **2015**, *27*, 5027−5031.
(33) Subramanian, A.; Tiwale, N.; Lee, W.-I.; Kisslinger, K.; Lu, M.; Stein, A.; Kim, J.; Nam, C.-Y. Vapor-Phase Infiltrated Organic-Inorganic Positive-Tone Hybrid Photoresist for Extreme UV Lithography. *Adv. Mater. Interfaces* **2023**, *10* (28), 2300420.
(34) Nam, C.-Y.; Stein, A.; Lu, M.; Kim, J.; Tiwale, N.; Hwang, S. M.; Subramanian, A. *Inorganic-Infiltrated Polymer Hybrid Thin Film Resists for Advanced Lithography*. US Patent US12140865B2, **2024**.
(35) Diulus, J. T.; Frederick, R. T.; Li, M.; Hutchison, D. C.; Olsen, M. R.; Lyubinetsky, I.; Arnadóttir, L.; Garfunkel, E. L.; Nyman, M.; Ogasawara, H.; et al. Ambient-Pressure X-ray Photoelectron Spectroscopy Characterization of Radiation-Induced Chemistries of Organotin Clusters. *ACS Appl. Mater. Interfaces* **2019**, *11*, 2526−2534.
(36) Ma, L.; Abney, C.; Lin, W. Enantioselective Catalysis with Homochiral Metal−Organic Frameworks. *Chem. Soc. Rev.* **2009**, *38*, 1248−1256.
(37) Zhang, X.; Huang, Z.; Ferrandon, M.; Yang, D.; Robison, L.; Li, P.; Wang, T. C.; Delferro, M.; Farha, O. K. Catalytic Chemoselective Functionalization of Methane in a Metal−Organic Framework. *Nat. Catal.* **2018**, *1*, 356−362.
(38) Chen, R.; Yao, J.; Gu, Q.; Smeets, S.; Baerlocher, C.; Gu, H.; Zhu, D.; Morris, W.; Yaghi, O. M.; Wang, H. A Two-Dimensional Zeolitic Imidazolate Framework With a Cushion-Shaped Cavity for CO_2 Adsorption. *Chem. Commun.* **2013**, *49*, 9500−9502.
(39) Zhong, Z.; Yao, J.; Chen, R.; Low, Z.; He, M.; Liu, J. Z.; Wang, H. Oriented Two-Dimensional Zeolitic Imidazolate Framework-L Membranes and their Gas Permeation Properties. *J. Mater. Chem. A* **2015**, *3*, 15715−15722.
(40) Kreno, L. E.; Leong, K.; Farha, O. K.; Allendorf, M.; Van Duyne, R. P.; Hupp, J. T. Metal−Organic Framework Materials as Chemical Sensors. *Chem. Rev.* **2012**, *112*, 1105−1125.
(41) Masih, D.; Chernikova, V.; Shekhah, O.; Eddaoudi, M.; Mohammed, O. F. Zeolite-like Metal−Organic Framework (MOF) Encaged Pt(II)-Porphyrin for Anion-Selective Sensing. *ACS Appl. Mater. Interfaces* **2018**, *10*, 11399−11405.
(42) Eslava, S.; Zhang, L.; Esconjauregui, S.; Yang, J.; Vanstreels, K.; Baklanov, M. R.; Saiz, E. Metal-Organic Framework ZIF-8 Films As Low-κ Dielectrics in Microelectronics. *Chem. Mater.* **2013**, *25*, 27−33.
(43) Conrad, S.; Kumar, P.; Xue, F.; Ren, L.; Henning, S.; Xiao, C.; Mkhoyan, K. A.; Tsapatsis, M. Controlling Dissolution and Transformation of Zeolitic Imidazolate Frameworks by using Electron-Beam-Induced Amorphization. *Angew. Chem. Int. Ed.* **2018**, *57*, 13592−13597.
(44) Miao, Y. R.; Tsapatsis, M. Electron Beam Patterning of Metal-Organic Frameworks. *Chem. Mater.* **2021**, *33*, 754−760.
(45) Tu, M.; Xia, B.; Kravchenko, D. E.; Tietze, M. L.; Cruz, A. J.; Stassen, I.; Hauffman, T.; Teyssandier, J.; De Feyter, S.; Wang, Z.; et al. Direct X-ray and Electron-Beam Lithography of Halogenated Zeolitic Imidazolate Frameworks. *Nat. Mater.* **2021**, *20*, 93−99.
(46) Miao, Y.; Lee, D. T.; de Mello, M. D.; Ahmad, M.; Abdel-Rahman, M. K.; Eckhert, P. M.; Boscoboinik, J. A.; Fairbrother, D. H.; Tsapatsis, M. Solvent-Free Bottom-Up Patterning of Zeolitic Imidazolate Frameworks. *Nat. Commun.* **2022**, *13* (1), 420.
(47) Liu, Q.; Miao, Y.; Villalobos, L. F.; Li, S.; Chi, H.-Y.; Chen, C.; Vahdat, M. T.; Song, S.; Babu, D. J.; Hao, J.; et al. Unit-Cell-Thick Zeolitic Imidazolate Framework Films for Membrane Application. *Nat. Mater.* **2023**, *22*, 1387−1393.
(48) Corkery, P.; Waltz, K. E.; Eckhert, P. M.; Ahmad, M.; Kraetz, A.; Miao, Y.; Lee, D. T.; Abdel-Rahman, M. K.; Lan, Y. C.; et al. Zinc-Imidazolate Films as an All-Dry Resist Technology. *Adv. Funct. Mater.* **2024**, *34* (12), 2311149.
(49) Park, K. S.; Ni, Z.; Cote, A. P.; Choi, J. Y.; Huang, R.; Uribe-Romo, F. J.; Chae, H. K.; O'Keeffe, M.; Yaghi, O. M. Exceptional Chemical and Thermal Stability of Zeolitic Imidazolate Frameworks. *Proc. Natl. Acad. Sci. U. S. A.* **2006**, *103*, 10186−10191.
(50) Tian, F.; Cerro, A. M.; Mosier, A. M.; Wayment-Steele, H. K.; Shine, R. S.; Park, A.; Webster, E. R.; Johnson, L. E.; Johal, M. S.; Benz, L. Surface and Stability Characterization of a Nanoporous ZIF-8 Thin Film. *J. Phys. Chem. C* **2014**, *118*, 14449−14456.
(51) Pan, Y.; Liu, Y.; Zeng, G.; Zhao, L.; Lai, Z. Rapid Synthesis of Zeolitic Imidazolate Framework-8 (ZIF-8) Nanocrystals in an Aqueous System. *Chem. Commun.* **2011**, *47*, 2071−2073.
(52) Stassen, I.; Styles, M.; Grenci, G.; Gorp, H. V.; Vanderlinden, W.; Feyter, S. D.; Falcaro, P.; Vos, D. D.; Vereecken, P.; Ameloot, R. Chemical Vapour Deposition of Zeolitic Imidazolate Framework Thin Films. *Nat. Mater.* **2016**, *15*, 304−310.
(53) Ma, X.; Kumar, P.; Mittal, N.; Khlyustova, A.; Daoutidis, P.; Mkhoyan, K. A.; Tsapatsis, M. Zeolitic Imidazolate Framework Membranes Made by Ligand-Induced Permselectivation. *Science* **2018**, *361*, 1008−1011.
(54) Lu, G.; Farha, O. K.; Zhang, W.; Huo, F.; Hupp, J. T. Engineering ZIF-8 Thin Films for Hybrid MOF-Based Devices. *Adv. Mater.* **2012**, *24*, 3970−3974.
(55) Levinson, H. J. High-NA EUV lithography: Current Status and Outlook for the Future. *Jpn. J. Appl. Phys.* **2022**, *61*, SD0803.
(56) Lorusso, G. F.; De Simone, D.; Zidan, M.; Severi, J.; Moussa, A.; Dey, B.; Halder, S.; Goldenshtein, A.; Houchens, K.; Santoro, G.; et al. e-Beam Metrology of Thin Resist for High NA EUVL. *Jpn. J. Appl. Phys.* **2023**, *62*, SG0808.
(57) Lorusso, G. F.; Beral, C.; Bogdanowicz, J.; De Simone, D.; Hasan, M.; Jehoul, C.; Moussa, A.; Saib, M.; Zidan, M.; Severi, J.et al. Metrology of Thin Resist for High NA EUVL. *Metrology, Inspection, and Process Control XXXVI* **2022**, *12053*, 120530O.
(58) IEEE. *International Roadmap for Devices and Systems, Executive Summary* **2022**.
(59) Hasan, R. M. M.; Luo, X. Promising Lithography Techniques for Next-Generation Logic Devices. *Nanomanuf. Metrol.* **2018**, *1*, 67−81.
(60) Waltz, K. E.; Eckhert, P. M.; Corkery, P.; Ahmad, M.; Kraetz, A.; Miao, Y.; Lee, D. T.; Abdel-Rahman, M. K.; Lan, Y.; Haghi-Ashtiani, P.et al. Amorphous Zinc-Imidazolate All-Dry Resists. *Advances in Patterning Materials and Processes XLI* **2024**, *12957*, 129570H.
(61) Pearton, S. J.; Shul, R. J.; Ren, F. A Review of Dry Etching of GaN and Related Materials. *MRS Internet J. Nitride Semicond. Res.* **2000**, *5* (1), 11.
(62) *Lam Research Teams Up with SK hynix to Enhance DRAM Production Cost Efficiency with Breakthrough Dry Resist EUV Technology*; Lam Research Corporation, 2022. https://www.prnewswire.com/news-releases/lam-research-teams-up-with-sk-hynix-to-enhance-dram-production-cost-efficiency-with-breakthrough-dry-resist-euv-technology-301567359.html (accessed 07 May 2025).
(63) *Breakthrough EUV Dry Photoresist Technology from Lam Research Adopted by Leading Memory Manufacturer.*; Lam Research Corporation, 2025. https://newsroom.lamresearch.com/2025-01-29-Breakthrough-EUV-Dry-Photoresist-Technology-from-Lam-Research-Adopted-by-Leading-Memory-Manufacturer (accessed 07 May 2025).
(64) Mack, C. Introduction to Semiconductor Lithography. In *Fundamental Principles of Optical Lithography*; Wiley, 2007; pp. 1−28.
(65) Mack, C. Photoresist Development. In *Fundamental Principles of Optical Lithography*; Wiley, 2007; pp. 257−296.
(66) Miao, Y.; Zheng, S.; Waltz, K. E.; Ahmad, M.; Zhou, X.; Zhou, Y.; Wang, H.; Boscoboinik, J. A.; Liu, L.; Agrawal, K. V.; et al. Spin-On Deposition of Amorphous Zeolitic Imidazolate Framework

(aZIF) Films for Lithography Applications. *Nat. Chem. Eng.* **2025**, *2* (9), 594−607.
(67) Waltz, K. E.; Eckhert, P.; Corkery, P.; Ahmad, M.; Kraetz, A.; Miao, Y.; Lee, D.; Abdel-Rahman, M.; Lan, Y.; Haghi-Ashtiani, P.et al. All-Dry Zinc-Imidazolate Resists for Electron Beam and EUV Lithography. *International Conference on Extreme Ultraviolet Lithography 2024* **2024**, *13215*, 132151D.
(68) Tian, X.; Li, F.; Tang, Z.; Wang, S.; Weng, K.; Liu, D.; Lu, S.; Liu, W.; Fu, Z.; Li, W.; et al. Crosslinking-Induced Patterning of MOFs by Direct Photo- and Electron-Beam Lithography. *Nat. Commun.* **2024**, *15* (1), 2920.
(69) Li, W.; Ma, T.; Tang, P.; Luo, Y.; Zhang, H.; Zhao, J.; Ameloot, R.; Tu, M. Nanoscale Resist-Free Patterning of Halogenated Zeolitic Imidazolate Frameworks by Extreme UV Lithography. *Adv. Sci.* **2025**, *12* (16), 2415804.
(70) Zhang, H.; Liu, D.; Yao, Y.; Zhang, B.; Lin, Y. S. Stability of ZIF-8 Membranes and Crystalline Powders in Water at Room Temperature. *J. Membr. Sci.* **2015**, *485*, 103−111.
(71) Choi, C.-H.; Su, Y.-W.; Chang, C.-H. Effects of Fluid Flow on the Growth and Assembly of ZnO Nanocrystals in a Continuous Flow Microreactor. *CrystEngComm* **2013**, *15*, 3326−3333.
(72) Ingavale, S.; Marbaniang, P.; Kakade, B.; Swami, A. Starbon with Zn-N and Zn-O Active Sites: An Efficient Electrocatalyst for Oxygen Reduction Reaction in Energy Conversion Devices. *Catal. Today* **2021**, *370*, 55−65.
(73) Tian, X.; Li, W.; Li, F.; Cai, M.; Si, Y.; Tang, H.; Li, H.; Zhang, H. Direct Photopatterning of Zeolitic Imidazolate Frameworks via Photoinduced Fluorination. *Angew. Chem. Int. Ed.* **2025**, *64* (1), e202500476.
(74) Butonova, S. A.; Ikonnikova, E. V.; Sharsheeva, A.; Chernyshov, I. Y.; Kuchur, O. A.; Mukhin, I. S.; Hey-Hawkins, E.; Vinogradov, A. V.; Morozov, M. I. Degradation Kinetic Study of ZIF-8 Microcrystals With and Without the Presence of Lactic Acid. *RSC Adv.* **2021**, *11*, 39169−39176.
(75) Pang, S. H.; Han, C.; Sholl, D. S.; Jones, C. W.; Lively, R. P. Facet-Specific Stability of ZIF-8 in the Presence of Acid Gases Dissolved in Aqueous Solutions. *Chem. Mater.* **2016**, *28*, 6960−6967.
(76) Xia, X.; Liu, J.; Xiao, Y.; Yu, Y.; Ren, Y.; Chen, J.; Xie, W.; Yang, B.; Zhang, J.; Yang, Z.; et al. Superhydrophobic Acid-Resistant Fluorinated ZIF-8 Prepared at Normal Temperature and Pressure. *Chem. Eng. J.* **2025**, *505*, 159223.
(77) Thakur, N.; Tseng, L.-T.; Vockenhuber, M.; Ekinci, Y.; Castellanos, S. Stability Studies on a Sensitive EUV Photoresist Based on Zinc Metal Oxoclusters. *J. Micro/Nanolithogr., MEMS, MOEMS* **2019**, *18* (4), 043504.
(78) Hotalen, J.; Murphy, M.; Earley, W.; Vockenhuber, M.; Ekinci, Y.; Freedman, D.; Brainard, R. L. Advanced Development Techniques for Metal-Based EUV Resists. *Extreme Ultraviolet (EUV) Lithography VIII* **2017**, *10143*, 1014309.
(79) Passarelli, J.; Cardineau, B.; Del Re, R.; Sortland, M.; Vockenhuber, M.; Ekinci, Y.; Sarma, C.; Neisser, M.; Freedman, D.; Brainard, R. L. EUV Resists Comprised of Main Group Organometallic Oligomeric Materials. *Advances in Patterning Materials and Processes XXXI* **2014**, *9051*, 90512A.
(80) Ramachandran, A. S.; Long, T.; Rodriguez, F. Evaluation of a New Zirconium-Containing, Negative-Working, Single-Layer Resist with Enhanced Oxygen and Fluorocarbon Reactive-ion Etch Resistance.*Advances in Resist Technology and Processing X* **1993**, *1925*, 400−406.
(81) Saifullah, M. S. M.; Rajak, A. K.; Hofhuis, K. A.; Tiwale, N.; Mahfoud, Z.; Testino, A.; Karadan, P.; Vockenhuber, M.; Kazazis, D.; Valiyaveettil, S.; et al. Approaching Angstrom-Scale Resolution in Lithography Using Low-Molecular-Mass Resists (<500 Da). *ACS Nano* **2024**, *18*, 24076−24094.
(82) Sortland, M.; Hotalen, J.; Del Re, R.; Passarelli, J.; Murphy, M.; Kulmala, T.; Ekinci, Y.; Neisser, M.; Freedman, D.; Brainard, R. L. Platinum and Palladium Oxalates: Positive-Tone Extreme Ultraviolet Resists. *J. Micro/Nanolithogr., MEMS, MOEMS* **2015**, *14* (4), 043511.
(83) Kenane, N.; Silva, A. D.; Haider, A.; Hoang, L.; Huang, C.-C.; Kam, B.; Kim, J. Y.; Lee, Y.; Li, D.; Tan, S.; et al. Dry Deposition and Dry Development of Metal Oxide Based Photoresist. *J. Photopolym. Sci. Technol.* **2024**, *37*, 257−262.
(84) Ogletree, D. F. Molecular Excitation and Relaxation of Extreme Ultraviolet Lithography Photoresists. In *Frontiers of Nanoscience*; Robinson, A.; Lawson, R., Eds.; Elsevier, 2016; Vol. *11*, pp. 91−113.
(85) Kostko, O.; McAfee, T.; Naulleau, P. Experimental Characterization of EUV Resist Materials: Photoelectron Spectroscopy. *Advances in Patterning Materials and Processes XXXIX* **2022**, *12055*, 1205508.
(86) Oyama, T. G.; Oshima, A.; Tagawa, S. Estimation of Resist Sensitivity for Extreme Ultraviolet Lithography Using an Electron Beam. *AIP Adv.* **2016**, *6* (8), 085210.
(87) Oyama, T. G.; Oshima, A.; Dang, T. N.; Enomoto, S.; Washio, M.; Tagawa, S. Prediction of Resist Sensitivity for 13.5-nm EUV and 6.x-nm EUV Extension From Sensitivity for EBL. *Extreme Ultraviolet (EUV) Lithography IV* **2013**, *8679*, 86792A.
(88) Singh, V.; Satyanarayana, V. S. V.; Batina, N.; Reyes, I. M.; Sharma, S.; Kessler, F.; Scheffer, F.; Weibel, D.; Ghosh, S.; Gonsalves, K. Performance Evaluation of Nonchemically Amplified Negative Tone Photoresists for e-Beam and EUV Lithography. *J. Micro/Nanolithogr., MEMS, MOEMS* **2014**, *13*, 043002.
(89) Wang, Z.; Chen, J.; Yu, T.; Zeng, Y.; Guo, X.; Wang, S.; Hu, R.; Tian, P.; Vockenhuber, M.; Kazazis, D.; et al. A Novel Water Developable Tetraphenyltin-Based Nonchemically-Amplified Molecular Resist for Sub-13 nm Lithography. *RSC Appl. Interfaces* **2024**, *1*, 544−551.
(90) Fallica, R.; Kazazis, D.; Kirchner, R.; Voigt, A.; Mochi, I.; Schift, H.; Ekinci, Y. Lithographic Performance of ZEP520A and mr-PosEBR Resists Exposed by Electron Beam and Extreme Ultraviolet Lithography. *J. Vac. Sci. Technol. B* **2017**, *35* (6), 061603.
(91) Chauhan, M.; Palit, K.; Choudhary, S.; Sharma, S.; Gonsalves, K. Ultrasensitive Metal-Organic Cluster Resist for Patterning of Single Exposure High Numerical Aperture Extreme Ultraviolet Lithography Applications. *J. Micro/Nanopattern. Mater. Metrol.* **2022**, *21*, 044603.
(92) Yuan, C.; Marui, R.; Adams, C.; Segalman, R. A.; Ober, C. K. Sequence-Defined Polypeptoids Facilitating Stochastics Control and EUV Patterning Study. *Advances in Patterning Materials and Processes XLII* **2025**, *13428*, 134281K.
(93) Bozano, L. D.; Brock, P. J.; Truong, H. D.; Sanchez, M. I.; Wallraff, G. M.; Hinsberg, W. D.; Allen, R. D.; Fujiwara, M.; Maeda, K. Bound PAG Resists: An EUV and Electron Beam Lithography Performance Comparison of Fluoropolymers. *Advances in Resist Materials and Processing Technology XXVIII* **2011**, *7972*, 797218.
(94) Shimizu, D.; Matsumura, N.; Kai, T.; Yamaguchi, Y.; Shimokawa, T.; Fujiwara, K. Performance Comparison of Chemically Amplified Resists Under EUV, EB, and KrF Exposure. *Advances in Resist Technology and Processing XXIII* **2006**, *6153*, 615344.
(95) Fallica, R.; Kirchner, R.; Ekinci, Y.; Mailly, D. Comparative Study of Resists and Lithographic Tools Using the Lumped Parameter Model. *J. Vac. Sci. Technol. B* **2016**, *34* (6), 06K702.
(96) Pollentier, I.; Neira, I.; Gronheid, R. Assessment of Resist Outgassing Related EUV Optics Contamination for CAR and non-CAR Material Chemistries. *Advances in Resist Materials and Processing Technology XXVIII* **2011**, *7972*, 797208.
(97) Takahashi, T.; Sugie, N.; Katayama, K.; Takagi, I.; Kikuchi, Y.; Shiobara, E.; Tanaka, H.; Inoue, S.; Watanabe, T.; Harada, T.et al. Resist Outgassing Characterization for Qualification in High Power EUV Lithography. *Extreme Ultraviolet (EUV) Lithography III* **2012**, *8322*, 83221E.
(98) Chang, S.-H.; Chen, S.-F.; Chen, Y.-Y.; Chien, M.-C.; Chien, S.-C.; Lee, T.-L.; Chen, J. J. H.; Yen, A. Balancing Lithographic Performance and Resist Outgassing in EUV Resists. *Extreme Ultraviolet (EUV) Lithography IV* **2013**, *8679*, 86790O.
(99) Dean, K. R.; Debeaux, G.; Wüest, A.; Garg, R. EUV Resist Outgassing: How Much is Too Much? *J. Photopolym. Sci. Technol.* **2007**, *20*, 393−402.

https://doi.org/10.1021/acs.chemmater.5c01476
Chem. Mater. 2025, 37, 8548−8567

(100) Hada, H.; Watanabe, T.; Hamamoto, K.; Kinoshita, H.; Komano, H. Evaluation of Resist Outgassing by EUV Irradiation.*Emerging Lithographic Technologies VIII* **2004**, *5374*, 686−694.
(101) Shiobara, E.; Takagi, I.; Kikuchi, Y.; Sasami, T.; Minegishi, S.; Fujimori, T.; Watanabe, T.; Harada, T.; Kinoshita, H.; Inoue, S. Recent Progress in EUV Resist Outgas Research at EIDEC. *J. Photopolym. Sci. Technol.* **2015**, *28*, 103−110.
(102) Santillan, J. J.; Kobayashi, S.; Itani, T. Outgassing Quantification Analysis of Extreme Ultraviolet Resists. *Jpn. J. Appl. Phys.* **2008**, *47*, 4922−4925.
(103) Levinson, H. *Principles of Lithography*; 4th ed.; SPIE Press, 2019.
(104) Fu, N.; Liu, Y.; Ma, X.; Chen, Z. EUV Lithography: State-of-the-Art Review. *J. Microelectron. Manuf.* **2019**, *2*, 19020202.
(105) Mueller, M. W.; McAfee, T.; Naulleau, P.; Oh, D.; Kostko, O. Outgassing Bond Structure, and Thickness in Polymers Under Electron Exposure. *Advances in Patterning Materials and Processes XLI* **2024**, *12957*, 129570C.
(106) Henke, B. L.; Gullikson, E. M.; Davis, J. C. X-ray Interactions: Photoabsorption, Scattering, Transmission, and Reflection at E = 50−30000 eV, Z = 1−92. *At. Data Nucl. Data Tables* **1993**, *54*, 181−342.
(107) Kostko, O. Update on Fundamental Studies of EUV Resists at CXRO.*Presented at the IEUVI Resist TWG Workshop*; San Jose McEnery Convention Center, 2024.
(108) Kostko, O.; McAfee, T. R.; Ma, J.; Blackwell, J.; Naulleau, P. Experimental Characterization of Model Resist Materials. *International Conference on Extreme Ultraviolet Lithography 2021* **2021**, *11854*, 1185407.
(109) Kwark, Y.-J.; Bravo-Vasquez, J. P.; Chandhok, M.; Cao, H.; Deng, H.; Gullikson, E.; Ober, C. K. Absorbance Measurement of Polymers at Extreme Ultraviolet Wavelength: Correlation Between Experimental and Theoretical Calculations. *J. Vac. Sci. Technol. B* **2006**, *24*, 1822−1826.
(110) Fallica, R.; Stowers, J.; Grenville, A.; Frommhold, A.; Robinson, A. P.; Ekinci, Y. Dynamic Absorption Coefficients of Chemically Amplified Resists and Nonchemically Amplified Resists at Extreme Ultraviolet. *J. Micro/Nanolithogr., MEMS, MOEMS* **2016**, *15*, 033506.
(111) Fallica, R.; Haitjema, J.; Wu, L.; Castellanos, S.; Brouwer, A. M.; Ekinci, Y. Absorption Coefficient of Metal-Containing Photoresists in the Extreme Ultraviolet. *J. Micro/Nanolithogr., MEMS, MOEMS* **2018**, *17* (02), 023505.
(112) Kostko, O.; McAfee, T.; Ma, J.; Blackwell, J.; Naulleau, P. Experimental Characterization of Model Extreme Ultraviolet Resist Materials. *J. Micro/Nanopattern. Mater. Metrol.* **2024**, *23*, 014602.
(113) Naaman, R.; Sanche, L. Low-Energy Electron Transmission Through Thin-Film Molecular and Biomolecular Solids. *Chem. Rev.* **2007**, *107*, 1553−1579.
(114) Jay-Gerin, J. P.; Plenkiewicz, B.; Plenkiewicz, P.; Perluzzo, G.; Sanche, L. Electron Mean Free Path and Conduction-Band Density-of-States in Solid Methane as Determined from Low-Energy Electron Transmission Experiments. *Solid State Commun.* **1985**, *55*, 1115−1118.
(115) Goulet, T.; Pou, V.; Jay-Gerin, J. P. A Procedure for Determining Low-Energy (<10eV) Electron Mean Free Paths in Molecular Solids: Benzene. *J. Electron Spectrosc. Relat. Phenom.* **1986**, *41*, 157−166.
(116) Torok, J.; Srivats, B.; Memon, S.; Herbol, H.; Schad, J.; Das, S.; Ocola, L.; Denbeaux, G.; Brainard, R. L. Electron Penetration Depths in EUV Photoresists. *J. Photopolym. Sci. Technol.* **2014**, *27*, 611−615.
(117) Jablonski, A.; Powell, C. J. Relationships Between Electron Inelastic Mean Free Paths, Effective Attenuation Lengths, and Mean Escape Depths. *J. Electron Spectrosc. Relat. Phenom.* **1999**, *100*, 137−160.
(118) Chang, Y. C.; Berry, W. B. Electron Range Studies in Solid Hydrocarbon Films at 77 K. *J. Chem. Phys.* **1974**, *61*, 2727−2735.
(119) Hino, S.; Sato, N.; Inokuchi, H. Electron Escape Depths of Organic Solids. *J. Chem. Phys.* **1977**, *67*, 4139−4144.
(120) Ma, J. H.; Naulleau, P.; Ahmed, M.; Kostko, O. Determination of Effective Attenuation Length of Slow Electrons in Polymer Films. *J. Appl. Phys.* **2020**, *127* (24), 245301.
(121) Kostko, O.; Mueller, M.; Naulleau, P. Evaluation of Electron Blur for Different Electron Energies. *J. Photopolym. Sci. Technol.* **2024**, *37*, 315−320.
(122) Fallica, R.; Mahne, N.; Conard, T.; Vanleenhove, A.; de Simone, D.; Nannarone, S. Mean Free Path of Electrons in Organic Photoresists for Extreme Ultraviolet Lithography in the Kinetic Energy Range 20−450 eV. *ACS Appl. Mater. Interfaces* **2023**, *15*, 35483−35494.
(123) Frederick, R. T.; Amador, J. M.; Goberna-Ferrón, S.; Nyman, M.; Keszler, D. A.; Herman, G. S. Mechanistic Study of HafSOx Extreme Ultraviolet Inorganic Resists. *J. Phys. Chem. C* **2018**, *122*, 16100−16112.
(124) Seah, M. P. Simple Universal Curve for the Energy-Dependent Electron Attenuation Length for All Materials. *Surf. Interface Anal.* **2012**, *44*, 1353−1359.
(125) Wagner, C.; Harned, N. Lithography Gets Extreme. *Nat. Photonics* **2010**, *4*, 24−26.
(126) Otsuka, T.; Kilbane, D.; White, J.; Higashiguchi, T.; Yugami, N.; Yatagai, T.; Jiang, W.; Endo, A.; Dunne, P.; O'Sullivan, G. Rare-Earth Plasma Extreme Ultraviolet Sources at 6.5−6.7 nm. *Appl. Phys. Lett.* **2010**, *97* (11), 111503.
(127) Tallents, G.; Wagenaars, E.; Pert, G. Lithography at EUV Wavelengths. *Nat. Photonics* **2010**, *4*, 809−811.
(128) Mojarad, N.; Vockenhuber, M.; Wang, L.; Terhalle, B.; Ekinci, Y. Patterning at 6.5 nm Wavelength Using Interference Lithography. *Extreme Ultraviolet (EUV) Lithography IV* **2013**, *8679*, 867924.
(129) Chkhalo, N. I.; Durov, K. V.; Nechay, A. N.; Perekalov, A. A.; Polkovnikov, V. N.; Salashchenko, N. N. On the Prospects of Lithography in the Region of Wavelengths Shorter than 13.5 nm. *J. Surf. Invest.: X-Ray, Synchrotron Neutron Technol.* **2023**, *17*, S226−S232.
(130) Anderson, C.; Ashworth, D.; Baclea-An, L. M.; Bhattari, S.; Chao, R.; Claus, R.; Denham, P.; Goldberg, K.; Grenville, A.; Jones, G.et al. The SEMATECH Berkeley MET: Demonstration of 15-nm Half-Pitch in Chemically Amplified EUV Resist and Sensitivity of EUV Resists at 6.x-nm. *Extreme Ultraviolet (EUV) Lithography III* **2012**, *8322*, 832212.
(131) Attwood, D. *Soft X-Rays and Extreme Ultraviolet Radiation: Principles and Applications*; Cambridge University Press, 1999.
(132) Kuznetsov, D. S.; Yakshin, A. E.; Sturm, J. M.; van de Kruijs, R. W. E.; Louis, E.; Bijkerk, F. High-Reflectance La/B-Based Multilayer Mirror for 6.x nm Wavelength. *Opt. Lett.* **2015**, *40*, 3778−3781.
(133) Fujimoto, U.; Harada, T.; Yamakawa, S.; Watanabe, T. Carbon/Boron Multilayer for Beyond EUV Lithography. *Photomask Japan 2023: XXIX Symposium on Photomask and Next-Generation Lithography Mask Technology* **2023**, *12915*, 129150M.
(134) Naujok, P.; Yulin, S.; Bianco, A.; Mahne, N.; Kaiser, N.; Tünnermann, A. La/B_4C Multilayer Mirrors with an Additional Wavelength Suppression. *Opt. Express* **2015**, *23*, 4289−4295.
(135) Yeh, J. J.; Lindau, I. Atomic Subshell Photoionization Cross Sections and Asymmetry Parameters: $1 \leqslant Z \leqslant 103$. *At. Data Nucl. Data Tables* **1985**, *32*, 1−155.
(136) Lüttgenau, B.; Zhang, M.; Zhang, Q.; Wang, C.; Ruiz, R.; Connolly, M.; Kostko, O. Time-Dependent Characterization of Total Electron Yield and Outgassing in Model EUV Resist Materials. *International Conference on Extreme Ultraviolet Lithography 2024* **2024**, *13215*, 132150H.
(137) Krull, X.; Tyler, C.; Neurock, M.; Hupp, J. Extension of Solvent-Assisted Linker Exchange to Supported Metal−Organic Framework Thin Films. *ChemRxiv* **2025**.

https://doi.org/10.1021/acs.chemmater.5c01476
Chem. Mater. 2025, 37, 8548−8567